Supporting Information

Self-Adhesive Flexible Electrocatalytic Patches of Stratified Oxide Heterojunctions with Engineered Band Alignments

Rasoul Khayyam Nekouei[1§*], Sajjad S. Mofarah[1§*], Samane Maroufi[1], Claudio Cazorla[2], Anthony P. O'Mullane[3], Yin Yao[4], and Veena Sahajwalla[1]

[1] Centre for Sustainable Materials Research and Technology, SMaRT@UNSW, School of Materials Science and Engineering, UNSW Sydney, NSW 2052, Australia

[2] Department of Physics, Polytechnic University of Catalonia, Campus Nord B4-B5, E-08034 Barcelona, Spain

[3] School of Chemistry and Physics, Queensland University of Technology (QUT), Brisbane, QLD 4001, Australia

[4] Electron Microscopy Unit (EMU)Mark Wainwright Analytical Centre UNSW Sydney, Australia

[*]Corresponding author, Email: r.nekouei@unsw.edu.au, s.seifimofarah@unsw.edu.au

Table of Contents

1. *Experimental*

1.1. Synthesis and fabrication procedure

The synthesis of free-standing, flexible, ZnO-based patches was based on the following steps (as thoroughly described in the next section): thermal reduction → evaporation → deposition → oxidation of ZnO and other oxides, *i.e.*, CdO, Bi_2O_3, and SnO_2, under controlled conditions in the absence of any catalyst. The source of ZnO, CdO, and SnO_2, was mainly from waste materials, respectively, from pure ZnO or electric arc furnace (EAF) dust with ≈50 wt% ZnO, end-of-life Ni-Cd battery, pure SnO_2 or waste lead-free soldering materials. Waste EAF dust was applied directly in the process, but some preparation steps, *i.e.*, physical separation and thermal treatment, were taken to prepare CdO and SnO_2 from waste sources. The desired amount of oxide/s powders, *e.g.*, 0.5 g, were placed at the centre of a graphite crucible with a graphitic lid. The filled crucible was placed on a graphite rod for insertion in an atmosphere-controlled horizontal (alumina) tube furnace, where the composition of the atmosphere, temperature, and evaporation time were controlled. The distance between the hot zone, where the crucible was inserted and hold, and the exhaust of the cold zone was 60-65 cm, as shown in **Fig. S1**. The production cycle included (a) holding 10 min in the cold zone, (b) fast insertion to the hot zone and holding for 5-10 min, (c) followed by pulling out and keeping in the cold zone for 10 min. We believe applying high temperature (1550°C) and high flow rate of carrier gas was made our process fast and efficient. Generally, the holding time in low-temperature processes in literature is more than 2-10 h[1,2], and inevitably the deposition took place on a prepared/standard substrate, such as Alumina plate[1], silicon wafer[2].

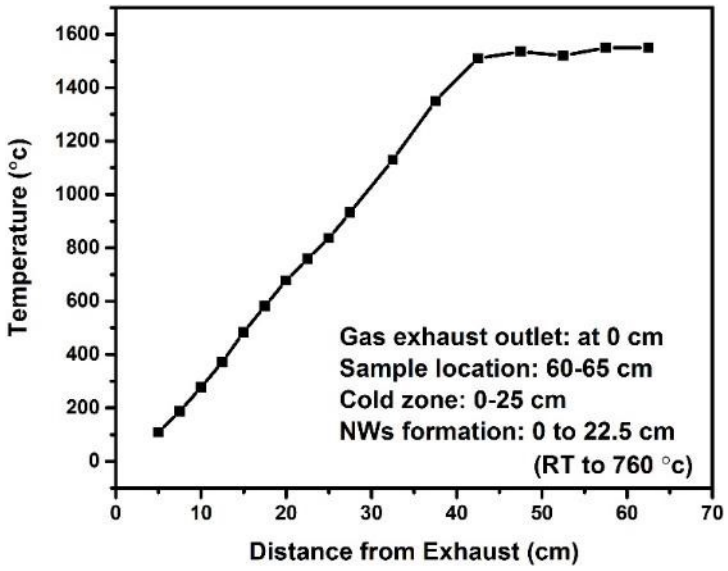

Fig. S1. The temperature profile of the horizontal tube furnace.

In a range of temperatures (1200-1550°C), only 1550°C was appropriate for the formation of flexible patches, which is owing to the desired temperature profile between the hot and cold zones in the furnace. Ar was purged from the back and O_2 from the front side of the tube (**Fig. 1**). The flow of Ar was changed from 1.6 to 80 $cm^3.s^{-1}$ to find the optimum flow for the desired patch properties, such as thickness and composition. The holding time in this research was significantly minimised, as low as 5-10 min, depending on the amount of oxide inside the crucible. Regardless of the composition, deposition of oxide/s patch took place on any existing surface in the cold zone, such as graphite, alumina, steel, without chemical bonding that made it easy to remove the patch from the surface. This patch was directly used for future characterisations.

1.2. Advanced characterisations

Transmission electron microscopy (TEM)

Dry powder of the specimens was suspended in water and ethanol and drop casted on a carbon-supported Cu grid followed by air-drying at room temperature. The prepared samples were used for TEM, scanning transmission electron microscopy (STEM), high angle annular dark-field

(HAADF), and energy dispersive spectroscopy (EDS) analysis. High-resolution transmission TEM (HRTEM) images and EDS analysis of the nanostructures were taken by a Philips CM 200 microscope (Eindhoven, the Netherlands), while HAADF imaging was conducted by JEOL JEM-ARM200F microscope (Tokyo, Japan). Both machines were operated at an accelerating voltage of 200 kV. Additionally, the beam flux was reduced to very low values of ~ 15 pA to minimise the beam damage effects. Finally, spectroscopy was conducted using spectrum imaging mode with sub-pixel scanning operative.

Scanning electron microscopy (SEM)

Scanning electron microscopy images were obtained by SEM (FEI Nova NanoSEM, Hillsboro, OR, USA) using secondary electron emission at accelerating voltage of 5 kV.

X-ray photoelectron spectroscopy (XPS)

Surface analysis of the ZnO and ZnO-based heterostructures were carried out using a Thermo Fisher Scientific ESCALAB 250Xi spectrometer (Loughborough, Leicestershire, UK) equipped with a monochromatic Al Kα source (1486.6 eV) hemispherical analyser. The chamber pressure was maintained < 8-10 mbar. All binding energies are referenced to the C1s signal corrected to 285 eV, and the spectra were fitted using a convolution of Lorentzian and Gaussian profiles.

X-ray diffraction (XRD)

Mineralogical data for the nanostructures were obtained using a Philips X'Pert Multipurpose X-ray diffractometer (Almelo, Netherlands) with CuKα radiation of 0.15405 nm, 2θ of 20°-80°, step size of 0.02°, and scanning speed of 5.5° 2θ min^{-1}. The peaks were analysed using X'Pert High Score Plus software (Malvern, UK).

Raman spectroscopy (Raman)

Raman analysis was carried out using a Renishaw inVia confocal Raman microscope (Gloucestershire, UK) equipped with a helium-neon green laser (514 nm) and diffraction

grating of 1800 g mm^{-1}. All Raman data were recorded at laser power of 35 mW and a spot size of ~2.0 μm. The data analysis was conducted by Renishaw WiRE 4.4 software and the calibration was done with respect to the silicon peak located at ~ 520 cm^{-1}.

Thermogravimetric analysis (TGA)

The decomposition behaviour of the ZnO patch was analysed by thermogravimetric analysis (TGA); TA Instruments, Q5000, 20°−1000°C, 20°C min^{-1} heating rate in air.

Atomic force microscopy (AFM)

The diameter of a single ZnO nanowire was measured by atomic force microscopy (AFM; Bruker Dimension Icon SPM, PeakForce Tapping mode). A ScanAsyst-Air probe (Bruker AFM probes) was installed in the AFM holder. The samples were deposited on glass, for AFM measurement, and silicon substrate, for KPAFM measurement, by applying a slight vacuum. The pixel resolution was 512 samples/line. A slow scan rate of 0.195 Hz was used to ensure accuracy.

Kelvin Probe Atomic Force Microscopy (KPAFM)

Amplitude modulated KPFM (AM-KPFM) measurement was performed using the Bruker Dimension ICON SPM with a Nanoscope V controller. A platinum-iridium coated AFM tip (SCM-PIT-V2, Bruker AFM probes) was used to scan the surface. The probe was firstly installed on a cantilever holder, and the laser was aligned onto the back of the cantilever. Then the probe was tuned near its resonance frequency with a small offset to the right-hand side of the resonance curve (typically for normal tapping mode image, we tune to the left side of the resonance curve, which makes the interaction force on the surface slightly repulsive. However, it was found for KPFM measurements, the offset to the right-hand side provided better results in selected specimens). The oscillation amplitude was kept around 30 to 40 nm, depending on the specimen. The amplitude setpoint and gains were adjusted accordingly for each specimen. The scan rate was around 0.3 to 0.4 Hz with a scan size of 10 μms and 512 samples per line as

the resolution. The scan setting included: Amplitude setpoint = 172 mV, gains = 1.1, scan rate = 0.326 Hz. Further, the operating parameters were as follows: The lift height was fixed at 50 nm for the specimens to avoid any influence from surface topography (sometimes a smaller lift height of 30 nm is used when scanning smaller areas). The drive2 amplitude of the AC bias applied to the tip during the lift pass was set to 500 mV with a 170° phase angle. Also, for calibration tests, which were done before and after measuring the specimen, the same AFM tip was also measured against a freshly cleaved HOPG sample and/or a pre-calibrated TiO_2 on a silicon reference sample. This calibration was important to determine the work function of the platinum tip, which can vary significantly from tip to tip.

UV-Vis spectroscopy

UV−Visible spectrometer (UV−Vis), PerkinElmer Lambda 1050, aperture 10 mm × 15 mm). The mass of the ZnO and ZnO-based heterojunction nanostructures were measured to be in the range of 10-12 mg.

Brunauer-Emmett-Teller (BET) analysis

After degassing step (micromeritics, VacPrep 061) at 180°C, Brunauer-Emmett-Teller (BET, micromeritics TriStar II 3020 V.3.0) method using 30 mg of the sample under liquid N_2 at 77.3 K was used to obtain BET surface area in $m^2.g^{-1}$ and pore size distribution caused by powder aggregating using Barrett-Joyner-Halenda (BJH) method.

1.3. Electrochemical application tests: H_2O_2 generation using catalytic patches

The patch was attached to the surface of fluorine-doped tin oxide (FTO) coated glass only by applying a homogenous mechanical pressure through a glass slide and without any binder (**Movie S2**). FTO coated glass with 600 nm FTO thickness, 6-9 Ω.square^{-1} resistance, 35 nm roughness, and 76% transparency was purchased from **Ossila**, UK. The surface area of FTO was 1.5×2.0 cm^2 that the patch was usually applied on 1.5×1.5 cm^2.

All electrochemical tests were carried out using a potentiostat/galvanostat workstation (**VSP-300**, BioLogic, USA). Linear voltammetry (LV), Electrochemical Impedance Spectroscopy (EIS), and Electrochemical active surface area (ECSA) were carried out in a standard three-electrode one-chamber cell. H_2O_2 was generated in a two-compartment cell in which a membrane (Nafion 117 from fuelcellstore.com, US, with 183 μm thickness and minimum 0.10 $S.cm^{-1}$ conductivity) separated two chambers filled with 40 ml of aqueous 2M $KHCO_3$ (Sigma-Aldrich) solution with pH of 8.3. The working electrode, reference electrode, and counter electrode were, respectively, the patch on FTO substrate, KCl saturated standard calomel electrode (SCE), and spiral Pt wire. According to literature[3,4], the potential was normalized using this equation: Potential (V) *vs*. RHE = Potential (V) *vs*. SCE + $0.24_{SCE \rightarrow SHE}$ + 0.059 × pH. All the electrochemical experiment in this research was conducted at room temperature. The amount of H_2O_2 was detected twice using a colourimetric method via H_2O_2 strips (Quantofix, **Peroxide 25**) and the average was reported. It is noteworthy that the measured H_2O_2 is lower than the generated since H_2O_2 is unstable under the applied potential, which leads to underestimated Faradic efficiency (FE)[4]. The FE of H_2O_2 was calculated via E_{S1}, as below:

$$\eta(H_2O_2) = \frac{2 \times Generated\ H_2O_2\ (mol)}{Passed\ charge\ (mol)} \times 100 \qquad E_{S1}$$

1.4. First-principles calculations / Density functional theory

Density functional theory (DFT)[5] calculations were performed to theoretically characterise the electronic properties (*i.e.*, bandgap and band alignments with respect to vacuum), and H_2O_2 catalytic activity of ZnO and the two 0D/3D heterojunction systems of Zn-Cd and Zn-Bi. The PBEsol exchange-correlation energy functional[6] was used as is implemented in the VASP software[7]. We employed the "projector augmented wave" method[8] to represent the ionic cores by considering the following electrons as valence: Zn 3*d* and 4*s*; Cd 4*d* and 5*s*; Bi 5*d* and 6p; O 2*s* and 2*p*; and H 1*s*. Wave functions were represented in a plane-wave basis truncated at 650 eV. For integrations within the first Brillouin zone, we employed Monkhorst-Pack k-point grids with a density equivalent to that of a 16x16x16 grid for the zinc-blende bulk ZnO unit cell. Periodic boundary conditions were applied along the three lattice vectors defining the simulation supercell; geometry relaxations were performed with a conjugate-gradient algorithm that optimised the ionic positions and volume and shape of the simulation cell. The relaxations were halted when the forces in the atoms were all below 0.01 eV·Å-1. By using these technical parameters, total energies were converged to within 0.5 meV per formula unit. The range-separated hybrid HSE06 exchange-correlation functional[9] was used to accurately estimate the electronic properties of the equilibrium oxide geometries previously determined with the PBEsol functional.

The theoretical value of the valence and conduction energy band edges of the 0D/3D ZnO-X (X = Cd and Bi) heterostructures as referred to the vacuum level were determined through the standard DFT approach described in work[10]. In a nutshell, both bulk and slab calculations were performed to obtain the alignment of the electrostatic potential within the analysed oxides by taking the vacuum level as reference. From the slab calculations, we obtained the macroscopic-average electrostatic potential within the semiconductors as referred to vacuum. The planar potential was computed by averaging potential values estimated within atomic planes oriented

perpendicular to the slab surface, while the macroscopic-average electrostatic potential was obtained by taking averages of the planar potential over distances of one unit cell along the same direction. For these calculations, simulation cells containing ~2.0 nm thick oxide slabs and 2.5 nm thick vacuum regions were employed. We checked that the electron density in the centre of the slabs was practically identical to those in the corresponding bulk materials. For the 0D/3D heterojunction systems of Zn-Cd- and Zn-Bi, we considered Cd and Bi interstitial atoms in the interior of zinc-blende ZnO for the bulk calculations, and Cd and Bi atoms adsorbed on a ZnO zinc-blende surface for the slab calculations.

The Zn-blende ZnO slab was Zn-terminated and cleaved along the (001) direction. The reasons for these choices are (1) the superior activities experimentally observed for Zn-terminated ZnO surfaces[11–13] and (2) the reconstruction of the polar (001) zinc-blende surface is technically simple and computationally efficient.

The adsorption Gibbs free energy of the intermediate reaction molecule HOO*, ΔGHOO*, was calculated for ZnO and the two heterojunction systems ZnO/CdO and ZnO/Bi_2O_3 by using the standard thermochemical formula[14,15]:

$$\Delta GHOO^* = \Delta EHOO^* + \Delta ZPE + T\Delta S \qquad E_{S2}$$

where ΔEHOO* is the binding energy of the HOO* molecule directly obtained from zero-temperature DFT calculations, ΔZPE the zero-point energy difference for the molecule adsorbed on the oxide surface and free in the gas phase, T the temperature, and ΔS the HOO* vibrational entropy difference for the molecule adsorbed on the oxide surface and free in the gas phase. The temperature was fixed to 300K in all our thermochemical calculations, and the VASPKIT code was used for postprocessing the data calculated with VASP[16].

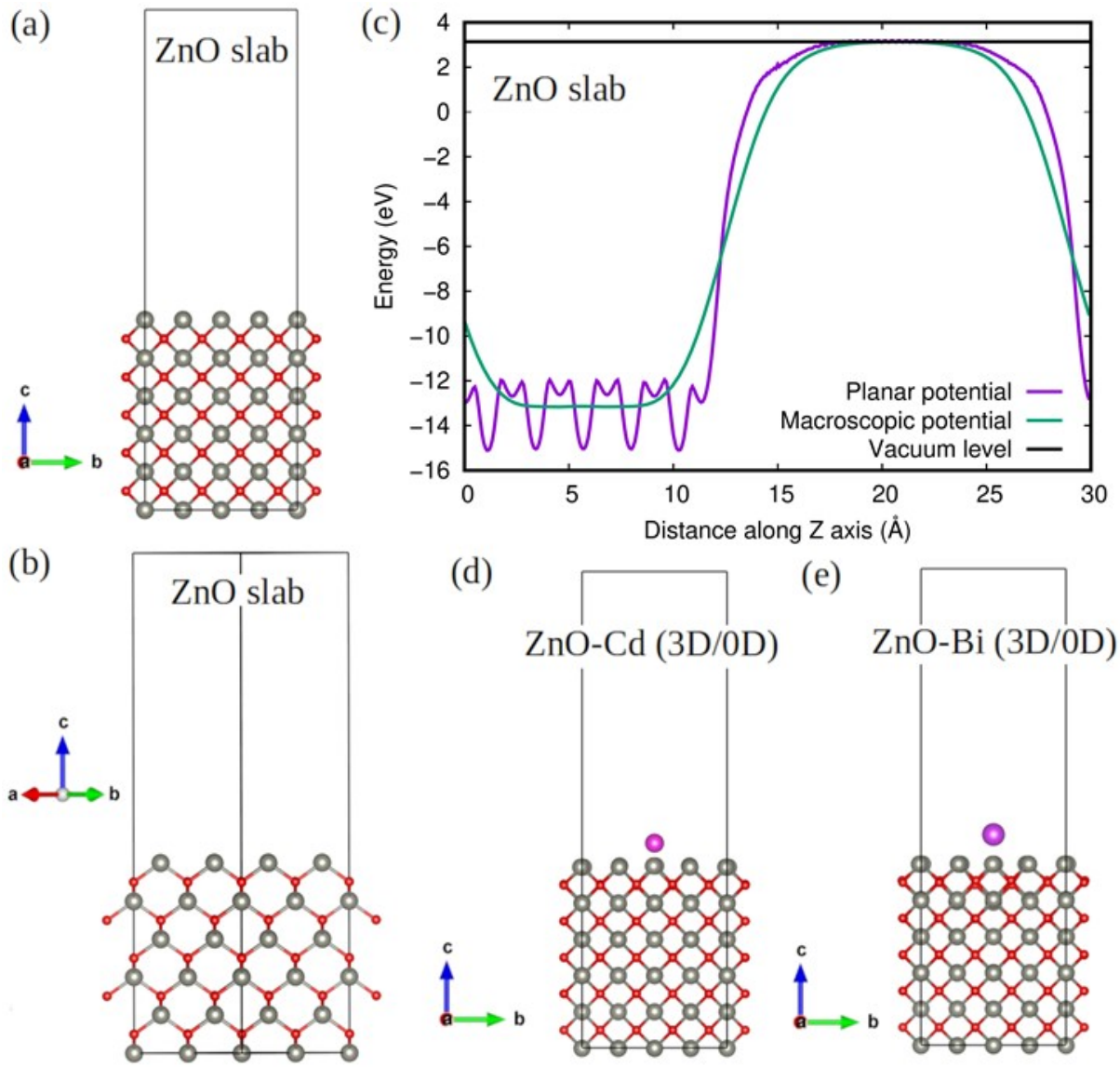

Fig. S2. (a)-(b) Atomic sketch of the reconstructed (001) zinc-blende ZnO slab employed in our DFT electronic band alignments and molecular HOO* adsorption calculations. (c) The reconstructed (001) zinc-blende ZnO slab is non-polar as evidenced by the zero-slope macroscopic potential (i.e., null internal electric field) estimated within the material. (d)-(e) Atomic sketch of the reconstructed (001) zinc-blende ZnO-X (X = Cd and Bi) slabs employed in our DFT electronic band alignments and molecular HOO* adsorption calculations. Zn, O, Cd and Bi atoms are represented with grey, red, magenta and violet spheres, respectively.

2. *Additional materials analysis*

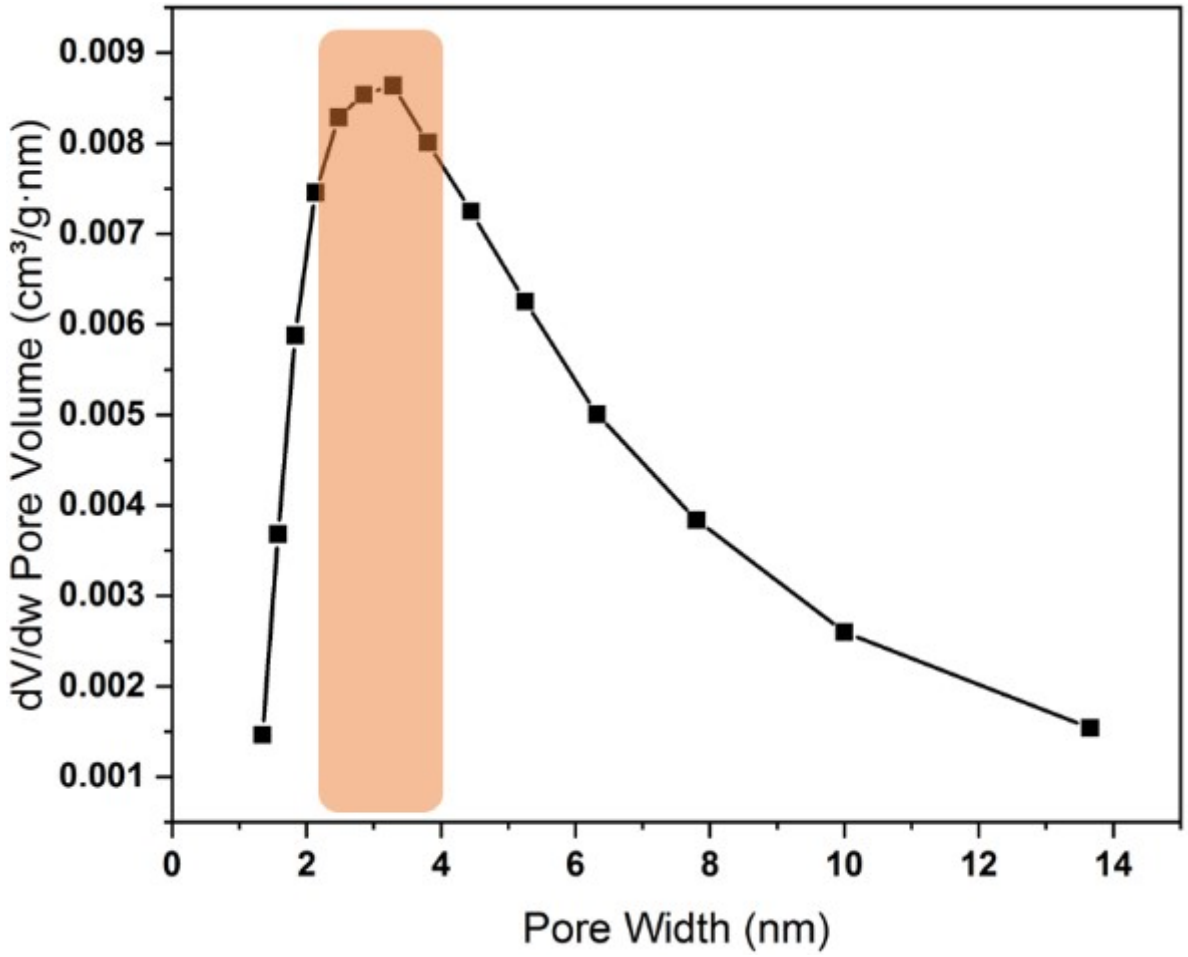

Fig. S3. BET physical adsorption plot of a ZnO patch made of NWs, with the BET surface area of 22.25 $m^2.g^{-1}$

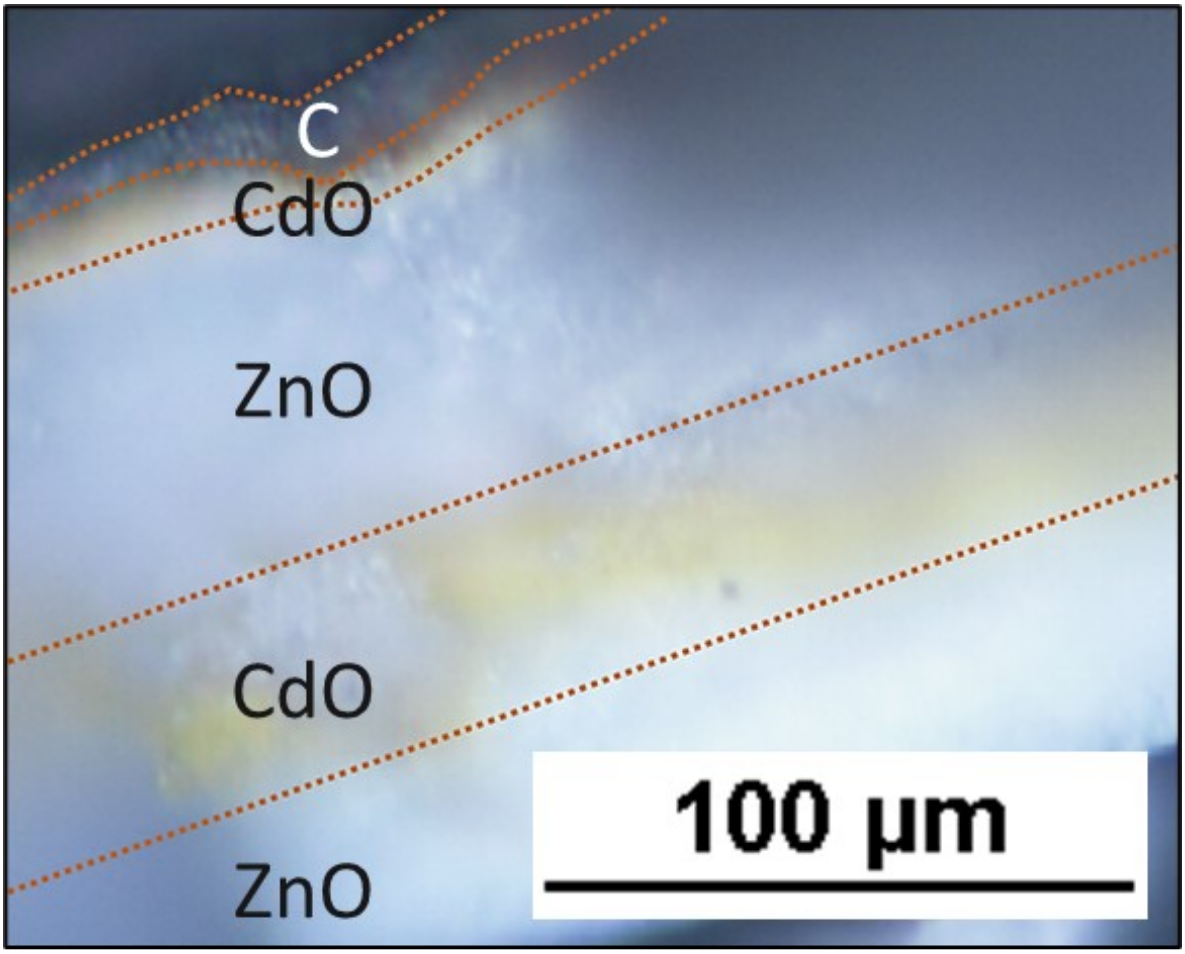

Fig. S4. Optical microscopy cross-section image of multilayer Zn-Cd-Zn-Cd-C heterojunction nanostructures.

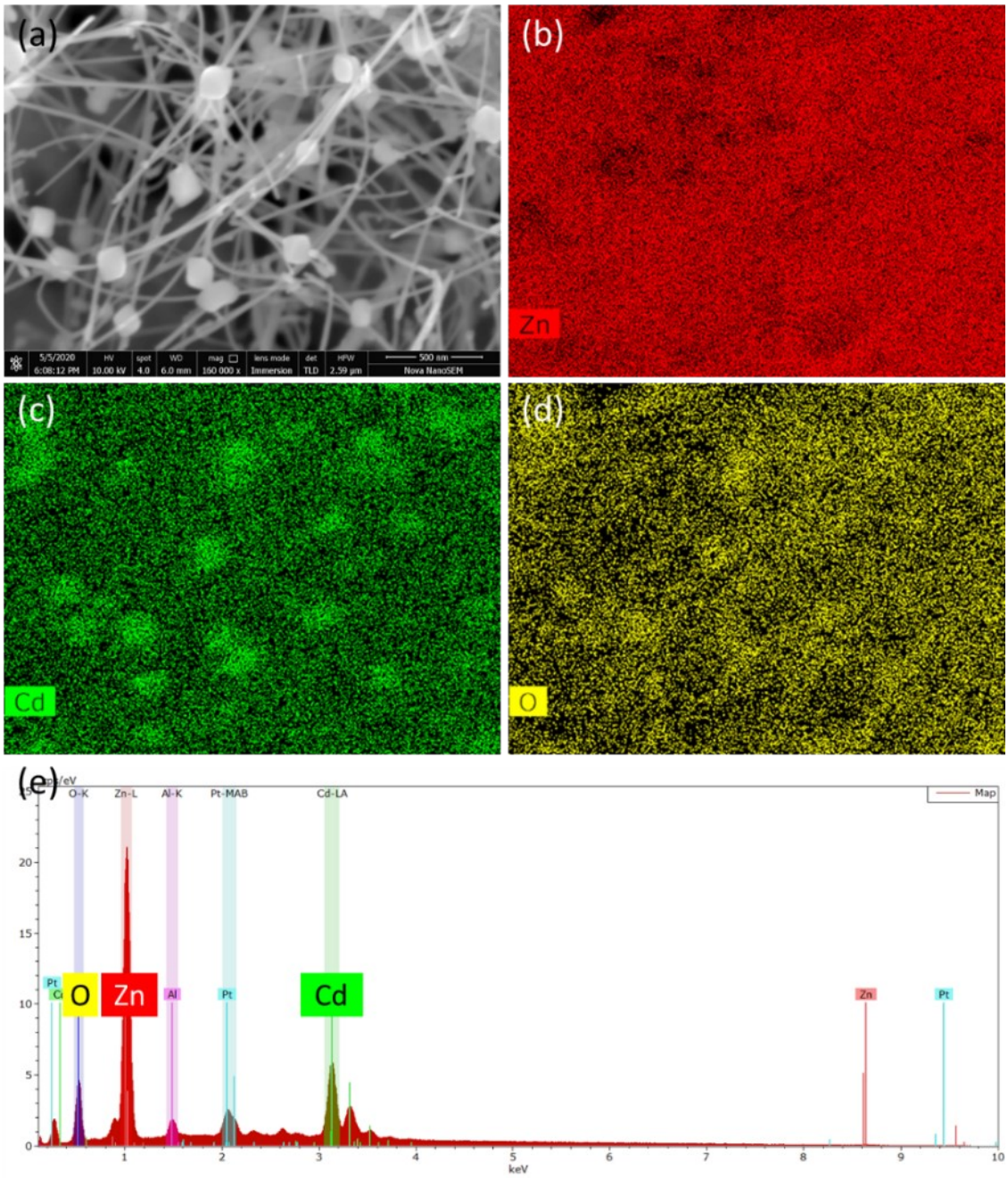

Fig. S5. EDS elemental analysis of the Zd-Cd heterojunction; **(a)** SEM image, **(b)** Zn, **(c)** Cd, and **(d)** O maps, and **(e)** EDS spectrum of the mapping elements.

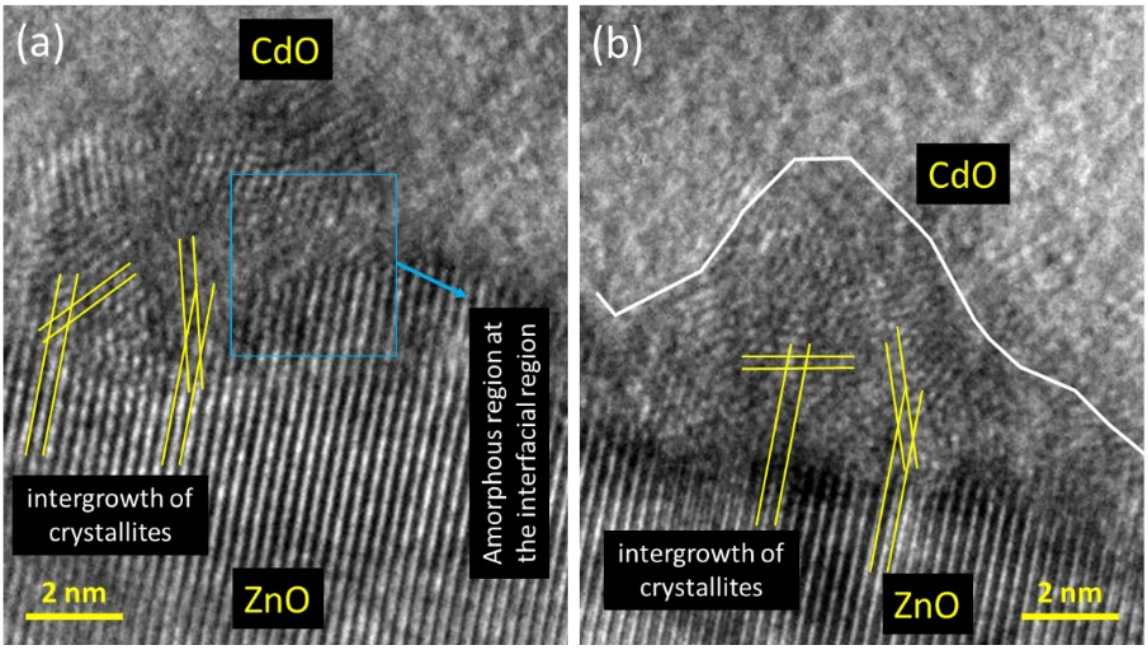

Fig. S6. HRTEM images of the Zn-Cd sample alongthe interface between ZnO single crystal nanoribbon and amorphous CdO spheres.

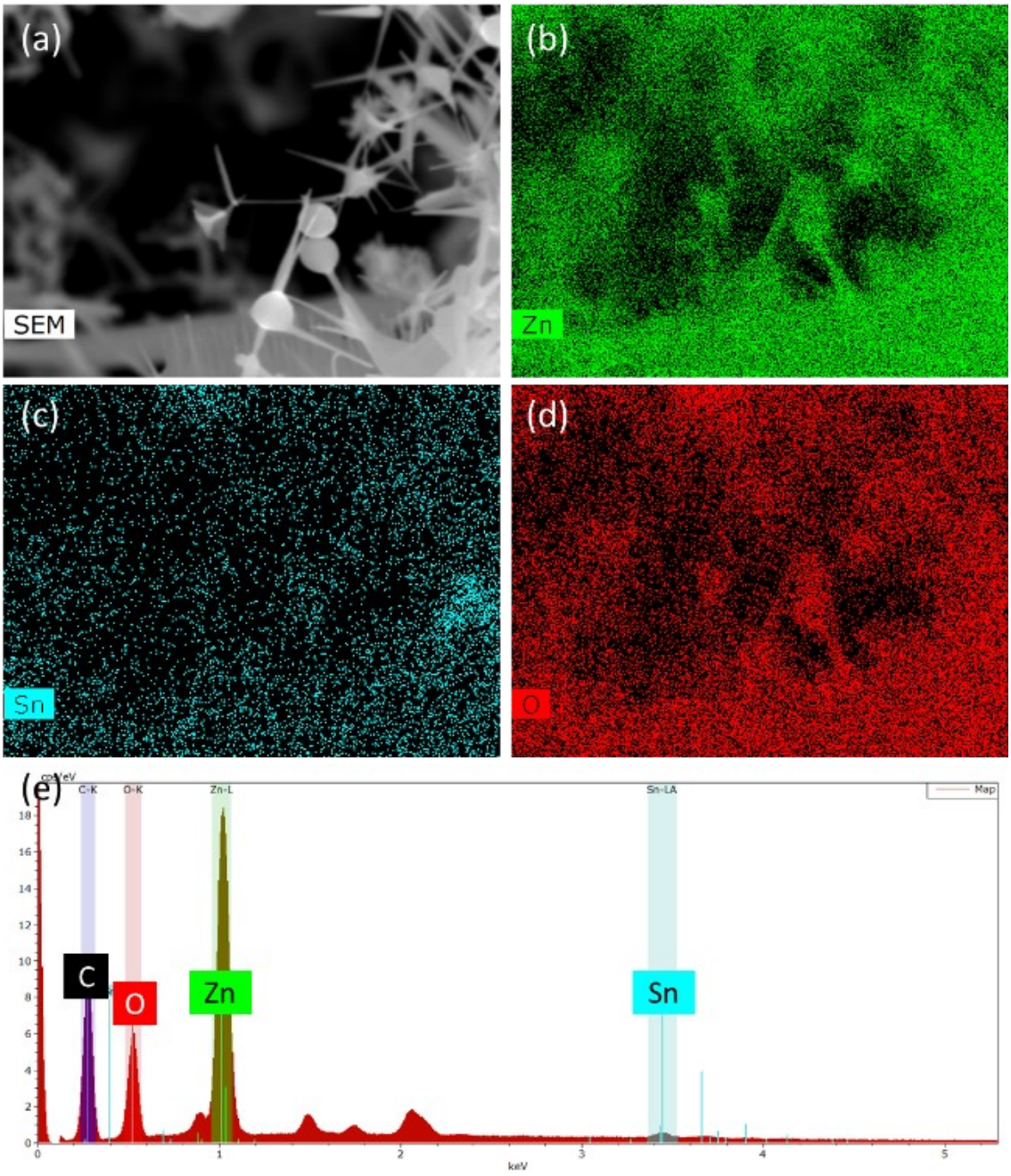

Fig. S7. EDS elemental analysis of the Zd-Sn heterojunction; **(a)** SEM image, **(b)** Zn, **(c)** Sn, and **(d)** O maps, and **(e)** EDS spectrum of the mapping elements.

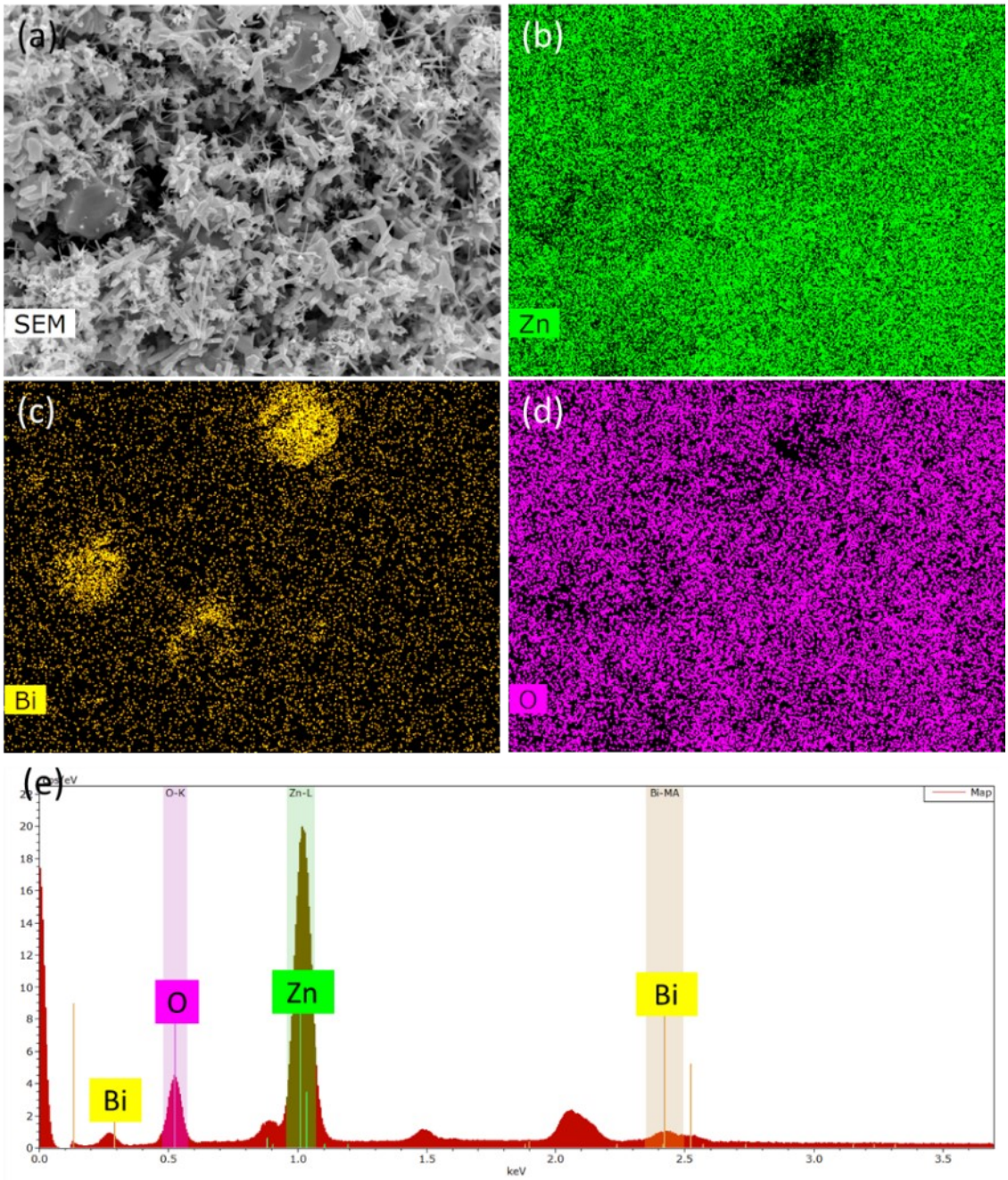

Fig. S8. EDS elemental analysis of the Zd-Bi heterojunction; **(a)** SEM image, **(b)** Zn, **(c)** Bi, and **(d)** O maps, and **(e)** EDS spectrum of the mapping elements.

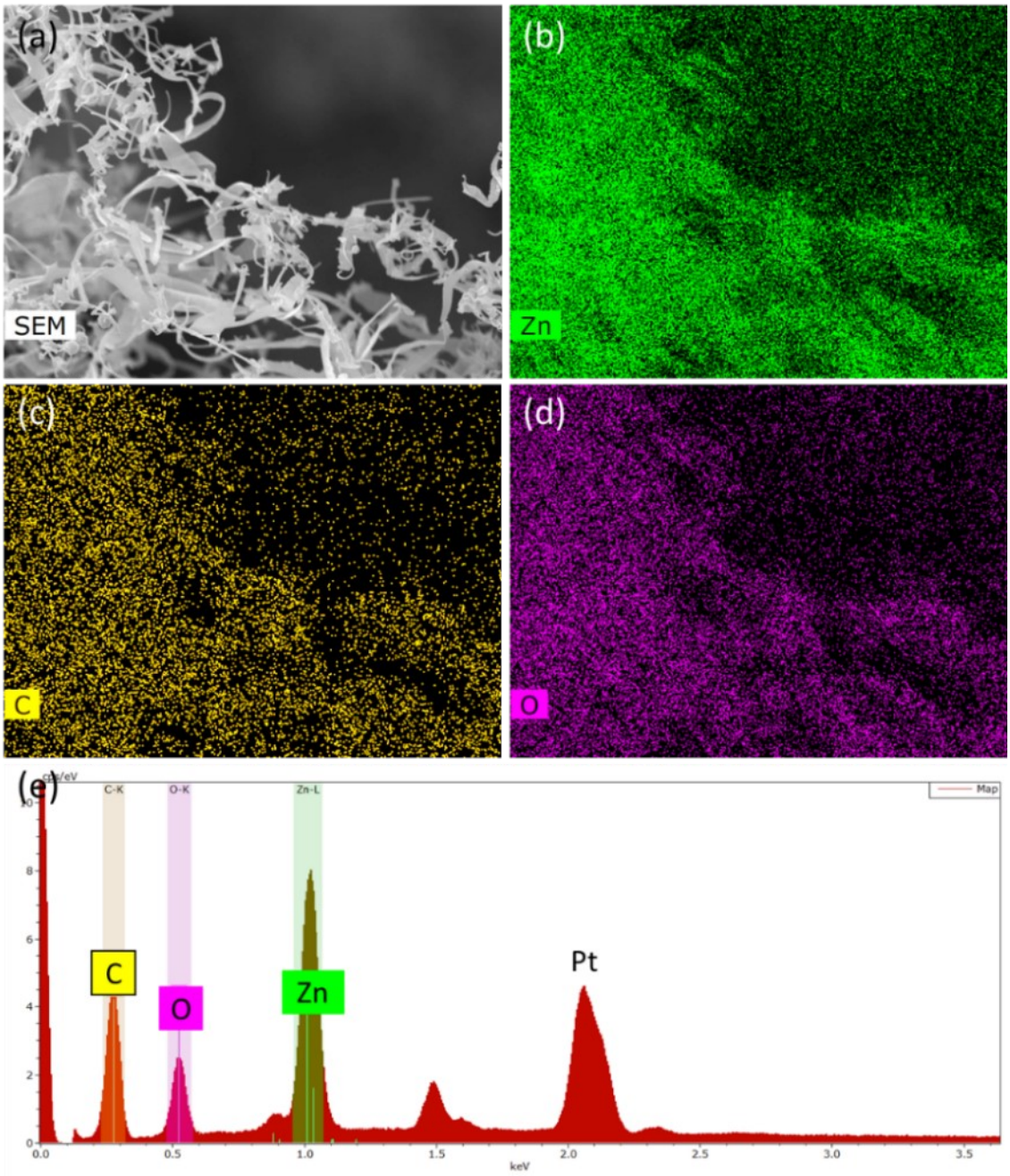

Fig. S9. EDS elemental analysis of the Zd-C heterojunction; **(a)** SEM image, **(b)** Zn, **(c)** C, and **(d)** O maps, and **(e)** EDS spectrum of the mapping elements.

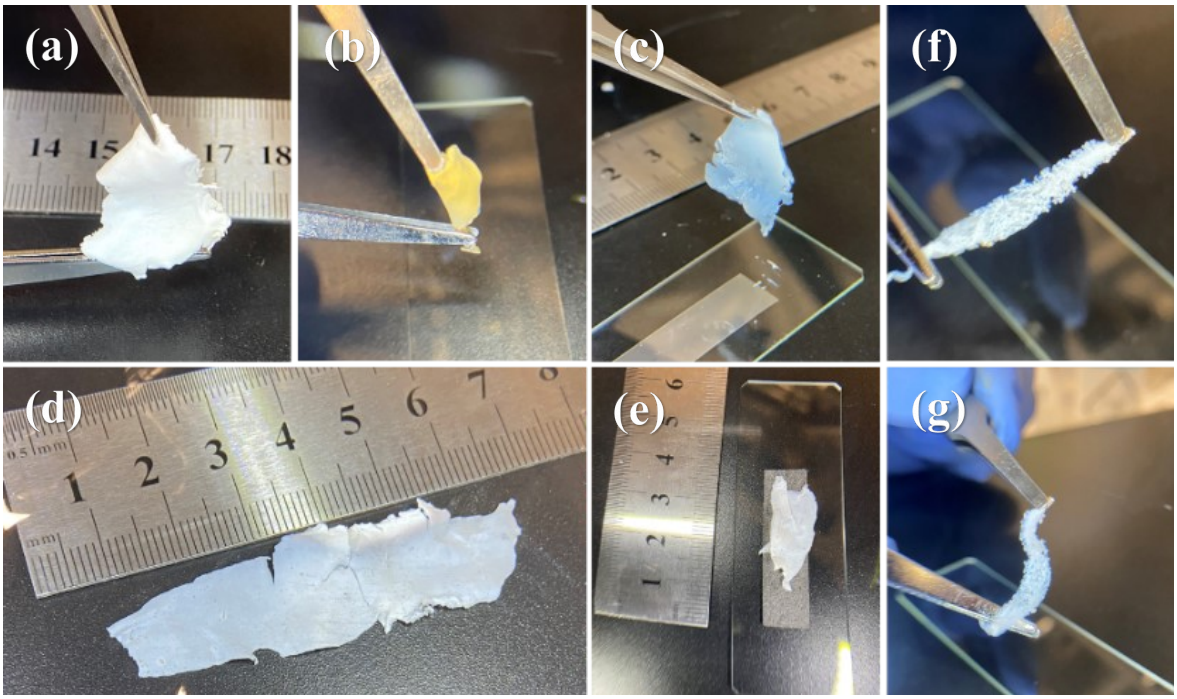

Fig. S10. Camera images from the centimetre-size, flexible, free-standing, ZnO-based heterojunction patches with different composition and shapes; **(a)** ZnO, **(b)** Zn-Cd, **(c)** Zn-C, **(d)** ZnO patch with a large macroscopic size/surface area, **(e)** ZnO patch attaching on a substrate using mechanical force via a glass plate, **(f-g)** flexibility of a macroscopic fibre-like ZnO patch under stretching (f) and twisting (g).

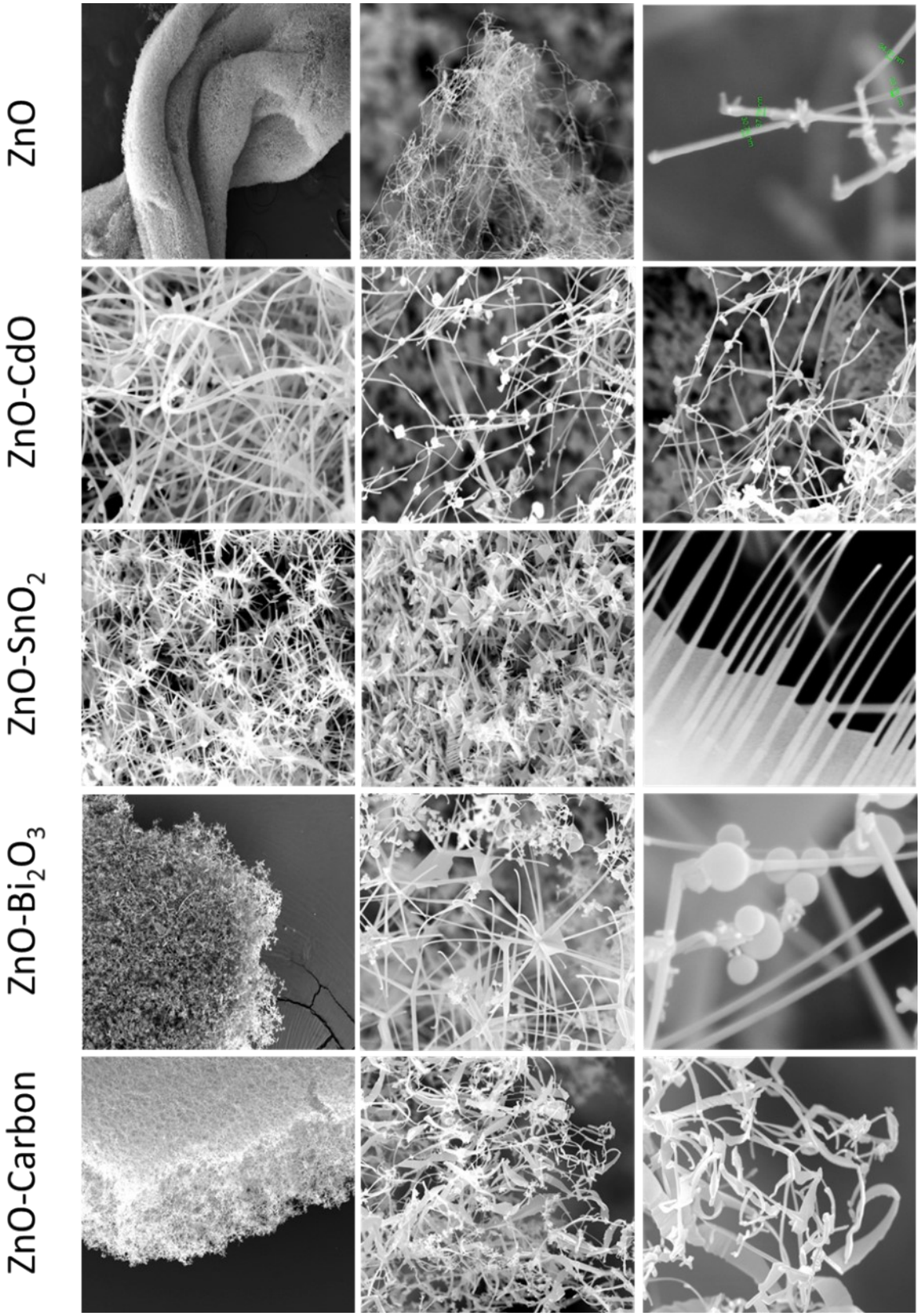

Fig. S11. Furthur FE-SEM images of the heterojunction patches made using different precursors under similar synthesis conditions for ZnO, Zn-Cd, Zn-Sn, Zn-Bi, Zn-C patches (from top to bottom).

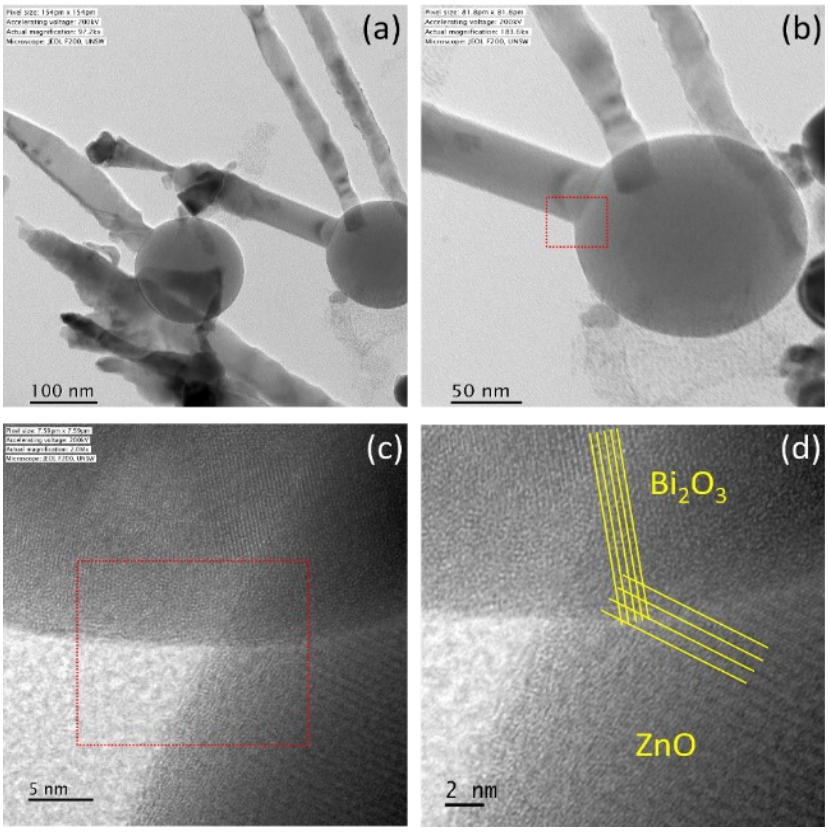

Fig. S12. HRTEM images of the Zn/Bi sample at the interface of ZnO and Bi_2O_3.

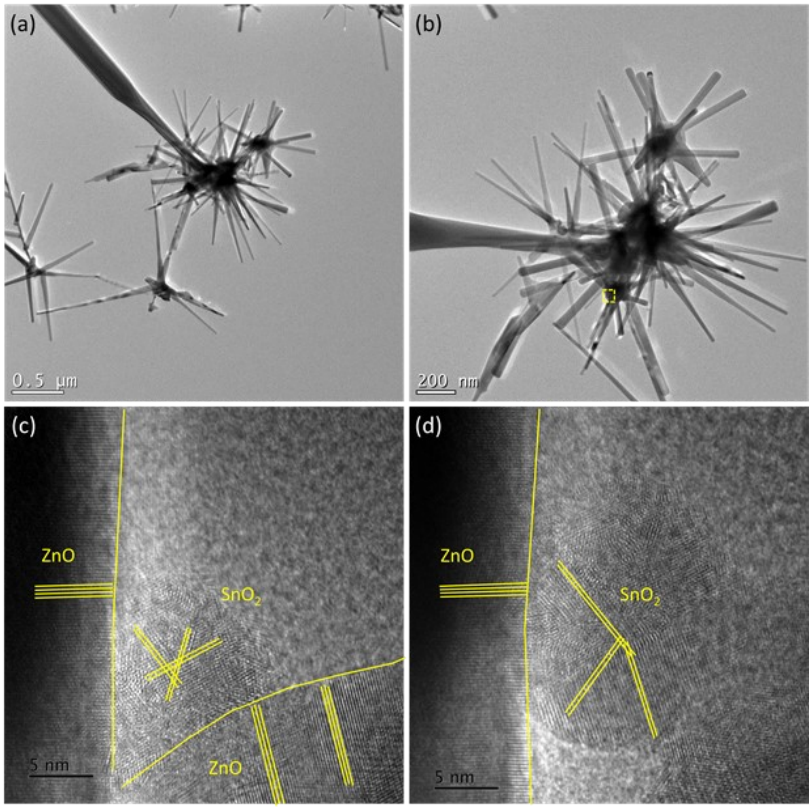

Fig. S13 (a,b) TEM and (c,d) HRTEM images of the Zn/Sn sample at the interface of ZnO and SnO_2.

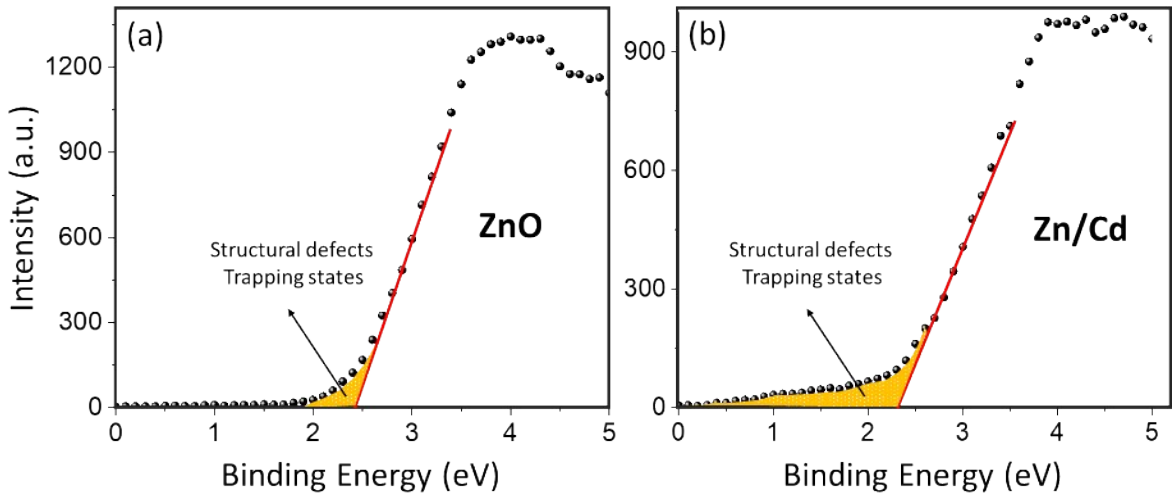

Fig. S14. XPS valence band analysis for ZnO and Zn/Cd samples.

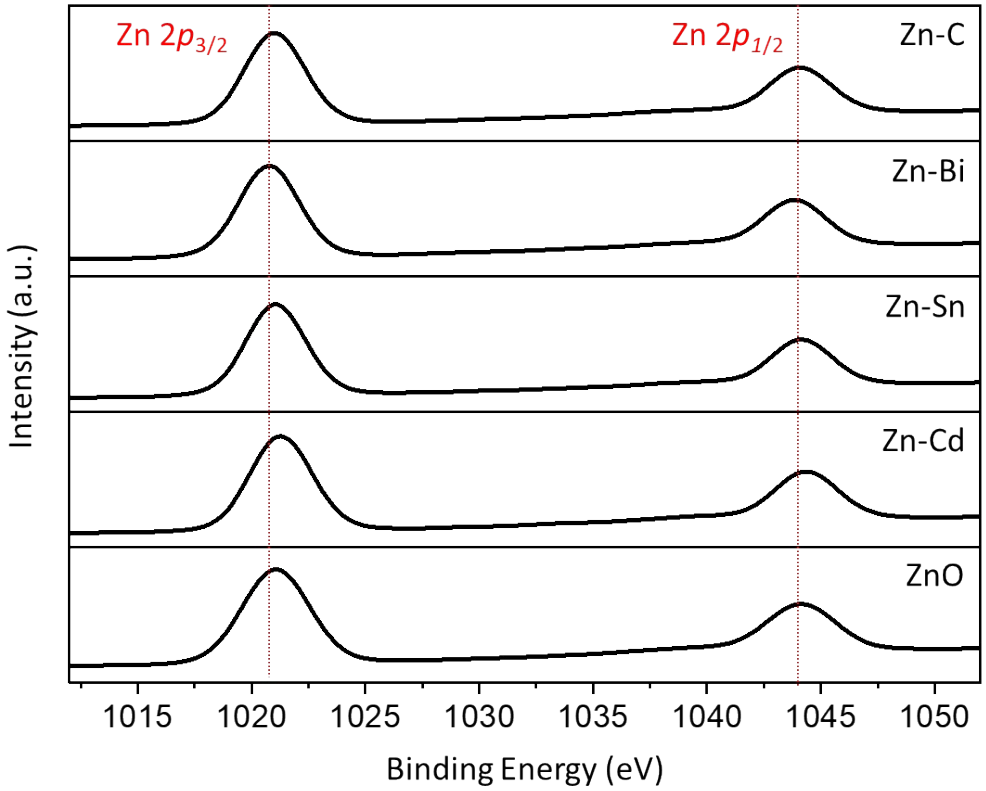

Fig. S15. XPS spectra for Zn 2p orbital of pristine ZnO and Zn-Cd, Zn-Sn, Zn-Bi, and Zn-C heterojunction nanostructures

.

3. Additional applications tests and literature review

Oxidative H_2O_2 production in electrochemical water splitting

H_2O_2 is among the top 100 utmost environmentally friendly and green redox chemicals[3], widely used in many industries[4,17] in the role of antibacterial, bleaching agent, antiseptic, selective organic converter, and an energy source in H_2O_2 fuel cells[18], leaving no pollutant behind[4,19]. Currently, 95% of H_2O_2 supply is produced via the well-known hydrogenation of anthraquinone and O_2 oxidation process[20] that is a multi-electron, energy-consuming process, which needs ample space and infrastructure[21]. Moreover, instability[3], storage, and transportation of H_2O_2 are regarded as safety concerns[20,21]. To date, establishing a system to generate and accumulate H_2O_2 using H_2O as raw material with high efficiency is noted as a breakthrough in clean chemical conversion processes[18] since this technology can decentralise the H_2O_2 production[4] and eliminate safety issues.

In recent years, tremendous attention has been attracted to H_2 generation from electrochemical (EC) or photo-electrochemical (PEC) water splitting (WS) for the search of renewable and sustainable fuels[22]; where H_2 is generated in the cathode (Re. S1) and the products of water oxidation reaction (WOR), i.e., $O_2/H_2O_2/OH^{\cdot}$, on the anode (*i.e.*, E_1-E_3 in the main text), regarding the applied potential[17].

$2H^+ + 2e^- \rightarrow H_2$ $\quad E° = 0$ V vs. RHE (Re. S1)

Therefore, WOR on anodic electrode includes three competing reactions which are as follows:

(1) Four-electron oxygen evolution reaction (E_1)

(2) Two-electron H_2O_2 evolution reaction (E_2)

(3) One-electron $OH^{\cdot}$ evolution reaction (E_3)

From the kinetics point of view, $OH^{\cdot}$ (hydroxyl radical) is not able to be generated in applied bias less than 3 V *vs*. RHE and WOR is governed by the slow-kinetics four-electron reaction, usually leading to O_2 evolution[17,22]. However, hydrogen peroxide (H_2O_2) with an economic

value of more than 20 times (in 2020) compared to O_2, is a significantly desired alternative product[17]. Both H_2O_2 and $OH^{\cdot}$ are oxidising agents and can be used as water disinfectant[23]; however, H_2O_2 is of interest due to being greener, safer, and using less potential.

Low-temperature electrosynthesis of H_2O_2, in which H_2O_2 directly is generated from water on the cathode or anode, can be an industrial alternative to the anthraquinone process and cost-effective on both large and small scales[20]. H_2O_2 can be formed under reducing potential on noble metal alloys or doped carbon cathode by partially reducing O_2[20]; however, the substantial barrier in the cathodic generation is dealing with the mixture of O_2 and H_2, which are potentially explosive over the range of 4-94mol% of H_2, resulting in a very diluted product[20]. Thus, the oxidative process seems safer and more attractive[4]. The development of new catalysts for oxidative H_2O_2 generation is complicated since most materials favour the evolution of O_2 on oxidative conditions[20]. On the other hand, the sluggish reaction kinetics and multi-electron process of WOR that needs an overpotential higher than 400 mV in oxygen evolution reaction (OER) (E_1), possibly activates H_2O_2 production (E_2) with the theoretical potential difference of 0.53 V[17]. To address the kinetic issues in oxidative process, developing new materials and structures to selectively and efficiently generates H_2O_2 is mandatory[21].

Catalysts for anodic oxidation are often transition metal oxides and free of noble metals[20]. Apart from the potent catalysts applied in PEC WOR[17], several promising oxide materials have been investigated in EC WOR, such as facet engineered ZnO[4], $BiVO_4$[21,22], SnO_2[3,21], TiO_2[21,22], WO_3[21,22], Al_2O_3[22,24], F-doped SnO_2 (FTO)[3,22,25], $CaSnO_3$[3], and Sb-containing mixed metal oxides[25], that all are less active/inactive for OER, which hints that well-defined OER catalysts such as RuO_2, IrO_2, Co, and Ni-based catalyst can be excluded for H_2O_2 production[17]. Thermodynamically, metal oxides that weakly bind oxygen intermediates, such as SnO_2 and TiO_2, can activate H_2O_2 evolution[19], while oxides such as PtO_2, RuO_2, and MnO_x[26] are proved that bind oxygen too strongly, inhibiting H_2O_2 generation or/and decompose it to O_2. To date,

our knowledge about the selectivity and activity of different metal oxides on energy barrier and limiting potential for H_2O_2 generation is little[21] and needs comprehensive theoretical and experimental data. In addition, severe degradation/corrosion of the electrode due to intensive oxidative environment during oxidative H_2O_2 generation makes it difficult to design a selective, stable, and efficient electrocatalyst[27]. Discovering highly durable candidates capable of generating and accumulating H_2O_2 in the electrolyte with high faradic efficiency (FE) needs systematically developing not only new materials/catalysts but also novel structures and surface modified catalysts[22]. Furthermore, these catalysts can be tuned through engineering the deposition of thin layers of different metal oxides[20,25].

Supporting experiments on H_2O_2 generation analysis

Water oxidative H_2O_2 production at low temperature introduced by Fuku et al. in 2016 [18] using hydrogen carbonate (HCO_3^-) electrolyte has opened a new horizon in this field. So far, the most promising results, in terms of FE and accumulation of H_2O_2, have been attained in 2M $KHCO_3$ electrolyte with pH of 7-8, since in alkaline electrolytes, the OER becomes dominant. Consequently, in this research, we utilised this electrolyte and used the following equation (Eq. S1) for FE of H_2O_2 [17,25,28].

$$\eta(H_2O_2) = \frac{2 \times Generated\ H_2O_2\ (mol)}{Passed\ charge\ (mol)} \times 100 \quad \text{(Eq. S1)}$$

In pH 7-8, the dominant species in bicarbonate system is HCO_3^-[18]. High concentration of HCO_3^- not only enhances the $\eta(H_2O_2)$ but also suppresses H_2O_2 degradation to O_2[18,22], increasing the accumulation of H_2O_2. The accumulated H_2O_2 in 2M $KHCO_3$ is reported to be 2.4 times larger than that of 1M $KHCO_3$[29]. Weakly acidic sites on the catalyst, such as TiO_2 and Al_2O_3[22], adsorb weakly basic HCO_3^- and enhance the oxidative H_2O_2 generation. After HCO_3^- oxidation on the surface of catalyst electrode at high applied potential, percarbonate species, i.e., HCO_4^- and

$C_2O_6^{2-}$, can be generated (Re. S2), followed by being hydrolysed by H_2O to form HCO_3^- and H_2O_2 (Re. S3), due to instability of percarbonates [2522]. HCO_3^- plays the role of a hole acceptor and turns into unstable HCO_4^- (Re. S2).

$HCO_3^- + H_2O \leftrightarrow HCO_4^- + 2(H^+ + e^-)$ $E° = +1.80$ V vs. RHE (Re. S2)

$HCO_4^- + H_2O \leftrightarrow H_2O_2 + HCO_3^-$ (Re. S3)

In a $KHCO_3$ solution/electrolyte, it has been reported that the applied potential has an insignificant impact on HCO_3^- oxidation during H_2O_2 generation, indicating a minor influence on the amount of generated H_2O_2[22] within the chosen potential windows.

The catalyst must also inhibit the decomposition of H_2O_2 since it readily decomposes to O_2 through self-degradation in the presence of a catalyst (Re. S4) or via hole oxidation (Re. S5). For instance, it has been shown that Al_2O_3[25] compared to $BiVO_4$, and $BiVO_4$[17] compared to bare FTO significantly suppresses H_2O_2 degradation. In addition, to avoid decomposition, the H_2O_2 molecule is expected to rapidly detach from the surface and diffuse away from the electrode before it undergoes further oxidation.[20]

$2H_2O_2 + \text{catalyst} \rightarrow O_2 + H_2O$ (Re. S4)

$H_2O_2 \rightarrow O_2 + 2H^+ + 2e^-$ $E^\circ = +0.68$ V *vs.* RHE (Re. S5)

The schematic of possible reactions, with their relevant potential, in water oxidation on the surface of the Zn-Cd heterojunction patch in 2M $KHCO_3$ is shown in **Fig. S16**.

The onset potential of oxidative reaction is critical in the overall efficiency of H_2O_2 generation. The two-electron oxidation reaction should represent high activity with low overpotential[21]. It is worth mentioning that different scan rates did affect the onset potential and current density insignificantly. As shown in **Fig. S17**, the onset potential of FTO shifts only 0.027 V from 50 to 200 $mV.s^{-1}$ scan rates.

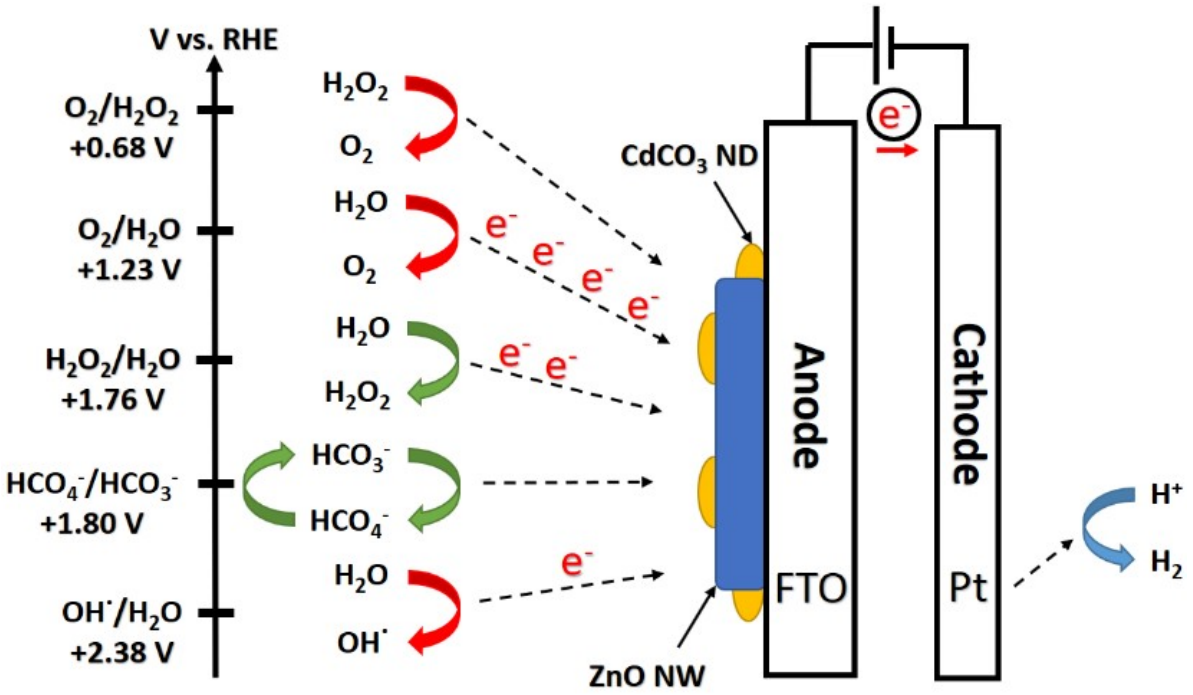

Fig. S16. Schematic of anodic reactions happen in the course of water oxidation process with the relevant potential vs. RHE. ZnO NW: ZnO nanowire; $CdCO_3$ ND: $CdCO_3$ nanodot.

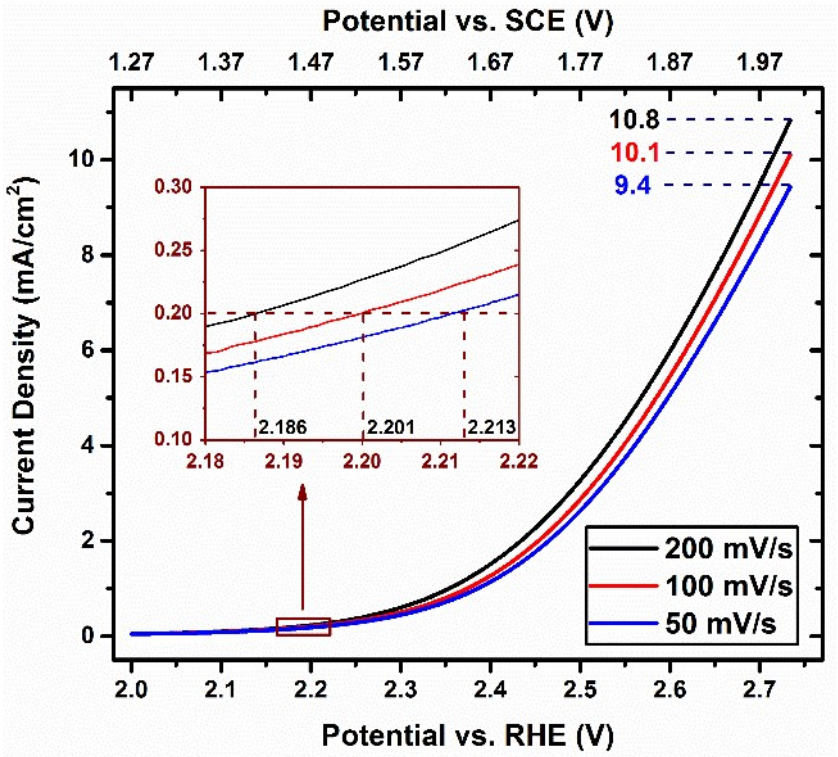

Fig. S17. Linear voltammetry (LV) of FTO at different scan rates (50-200 $mV.s^{-1}$) in a one-compartment cell, 2M $KHCO_3$, room temperature, and Pt as the counter electrode.

For in-depth analysis of surface behaviour of the catalyst at increasing potentials, electrochemical impedance spectroscopy (EIS) tests were carried out on FTO and Zn-Cd patch at four different potentials, as represented in **Fig. S18**. In OCV, Zn-Cd patch shows a very high resistance that is attributed to the insulation behaviour of $CdCO_3$ and ZnO on the surface, which block the passage of electrons. After applying the potential (1.73 V), both catalysts resistance intensifies, which might be because of the formation of electrochemical layers. Once the potential increases to 1.93 V (that is the onset potential for Zn-Cd patch), the resistance of the Zn-Cd patch plunges faster than FTO. Eventually, at 2.33 V, both catalysts have enough activity that leads to a significant drop in resistance, although the Zn-CdOpatch offers better conductivity, confirming its higher current density.

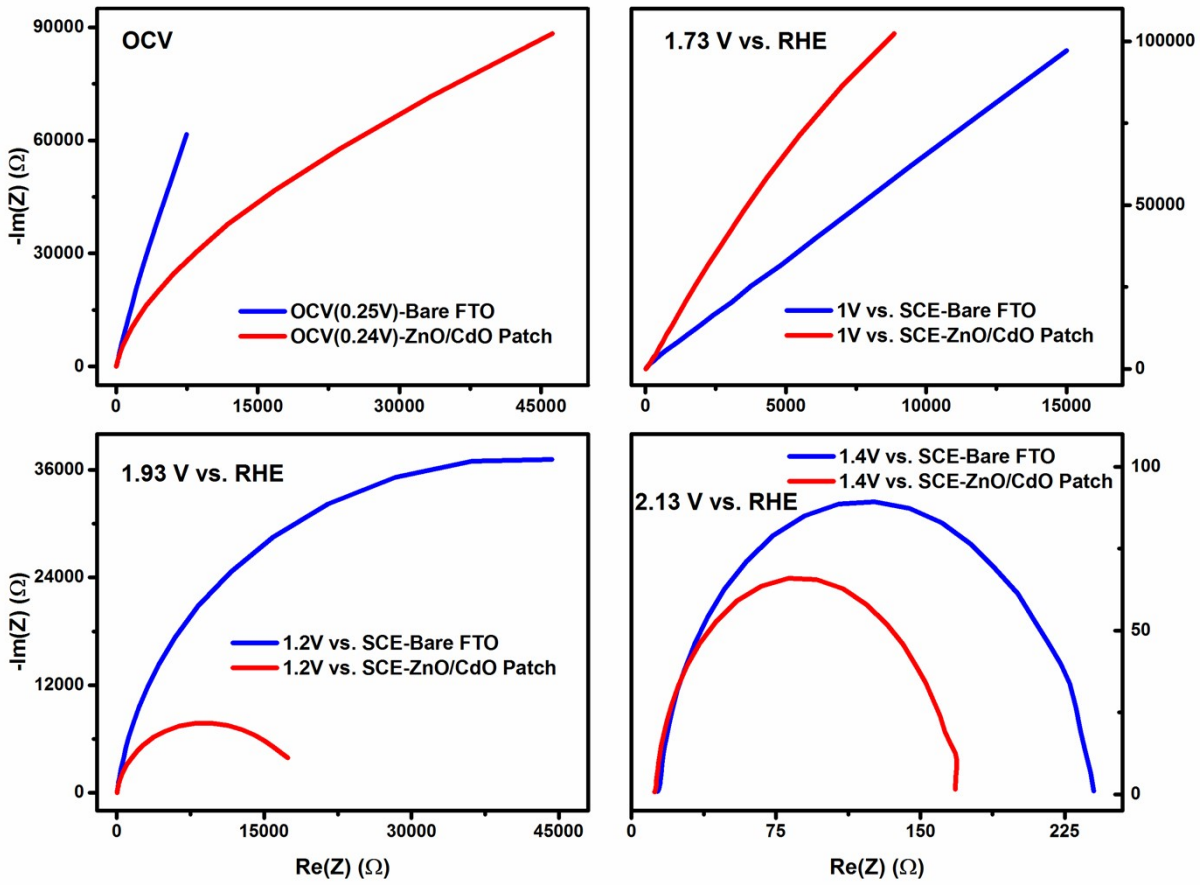

Fig. S18 Electrochemical impedance spectroscopy (EIS) of FTO and Zn-Cd patch at four different potentials, *i.e.*, OCV, 173, 1.93, and 2.33 V *vs.* RHE, in the range of 100 kHz to 100 mHz and 10 mV amplitude, in a two-compartment cell, 2M $KHCO_3$, room temperature, and Pt as the counter electrode.

Fig. S19 shows ECSA results for both catalysts between 1.23 to 1.33 V *vs*. RHE at five scan rates as plotted in **Fig. S19a-b**, using $i_c = \nu C_{dl}$, where i_c, ν, and C_{dl} are double-layer capacitive current, scan rate, and double-layer capacitance[30]. The current density at 1.28 V *vs*. RHE was taken for plotting current density *vs*. scan rate.

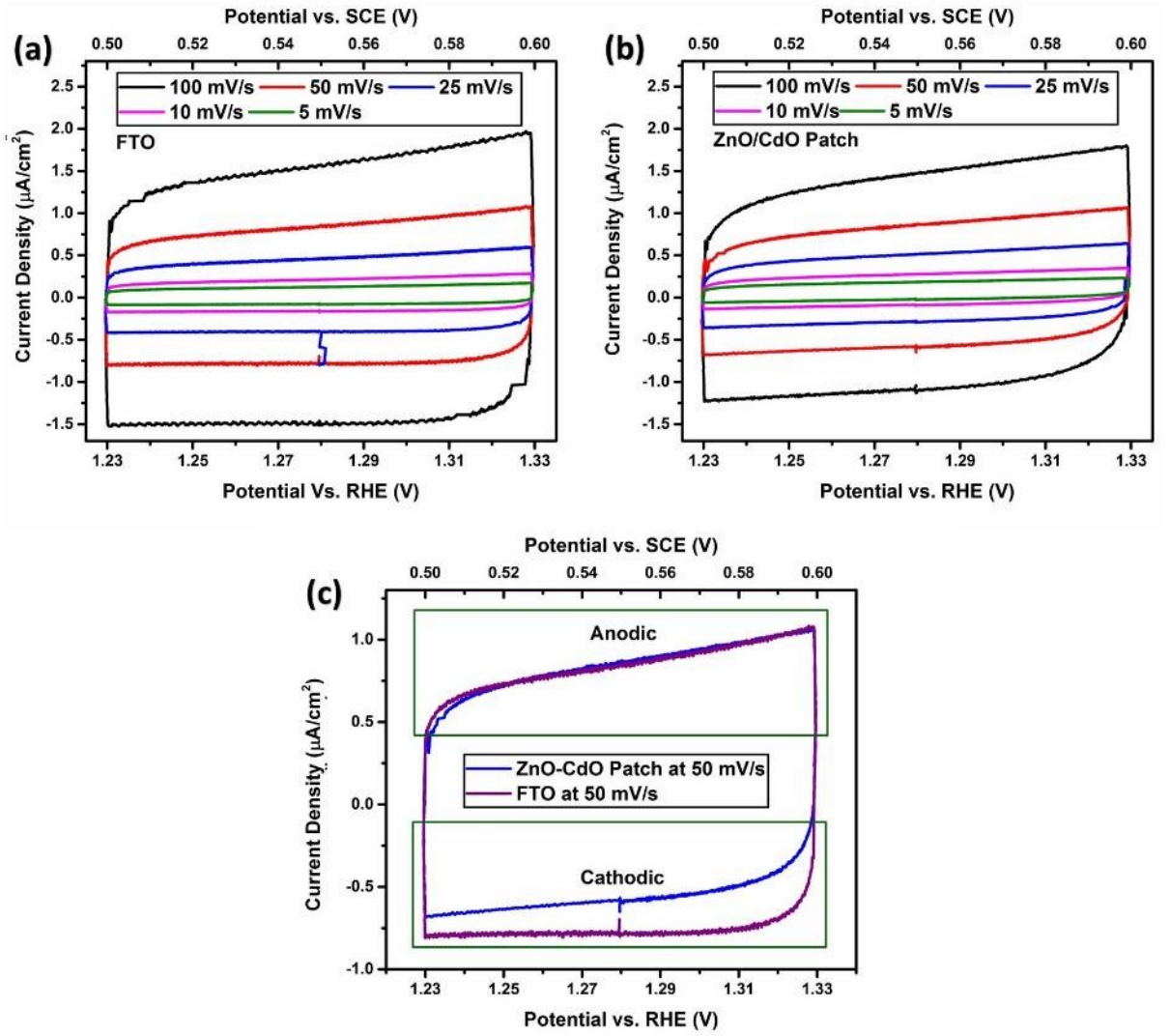

Fig. S19 Electrochemical surface area (ECSA) measurement between 1.23 to 1.33 V *vs*. RHE at five different scan rates for **(a)** FTO, and **(b)** Zn-Cd heterojunction patch as working electrode; **(c)** a comparison between the CV for FTO and Zn-Cd patch at 50 $mV.s^{-1}$, in a two-compartment cell, 2M $KHCO_3$, room temperature, and Pt as the counter electrode.

The XRD analysis (**Fig. S20**) confirmed the phase transition, during which the exposure of Zn-Cd patch with $KHCO_3$ solution results in rapid CdO transformation into $CdCO_3$. This possible mechanism is thoroughly shown in **Fig. S16**. Further, the colour change from orange to white confirms such transformation. This transformation seems beneficial since the adherence of the patch becomes stronger, and the patch is more stable. This transformation is shown to be reversible, and the thin film easily returns to CdO after heat treating at 200°C on a hotplate for 10 min.

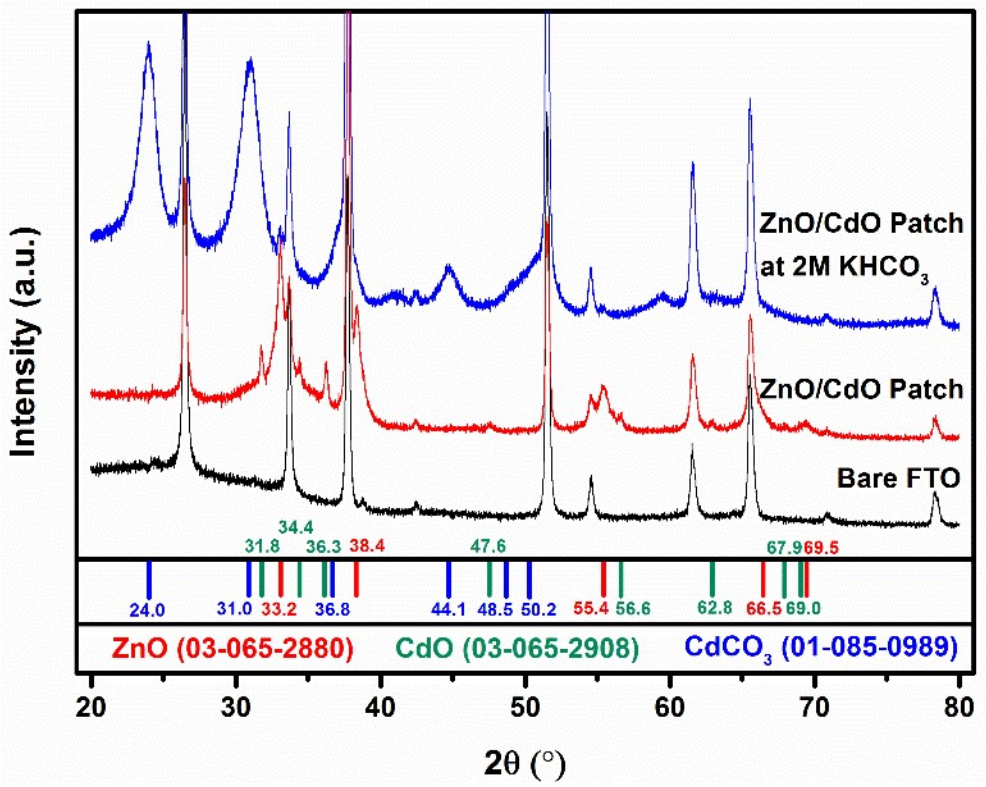

Fig. S20. XRD patterns and relevant analysis, including the allocated peaks to recognised phases, of FTO and ZnO-CdO heterojunction patch before and after the exposure to $KHCO_3$.

Stability and endurance of the electrocatalyst at such high potentials[3], as well as the accumulation of H_2O_2 in the solution, are other critical criteria that are governed by the oxidation potential and pH of the electrolyte[23]. Only a few materials can withstand such oxidising conditions for the long run[4]. The catalyst must not dissolve and maintain its activity

over time. Previous studies confirmed that the mixed/ternary metal oxides such as $CaSnO_3$[3], $Al_2O_3/BiVO_4$[24], $WO_3/BiVO_4$[18], and Sb-containing mixed metal oxides[25] are more efficient and stable[3], leading us to choose mixed oxides for this research. In literature, the chemical mixture or layered of two or three different oxides have been applied that in most cases, the results were more promising than just one single metal oxides, while, to the best of our knowledge, no heterojunction in nanoscale has been investigated.

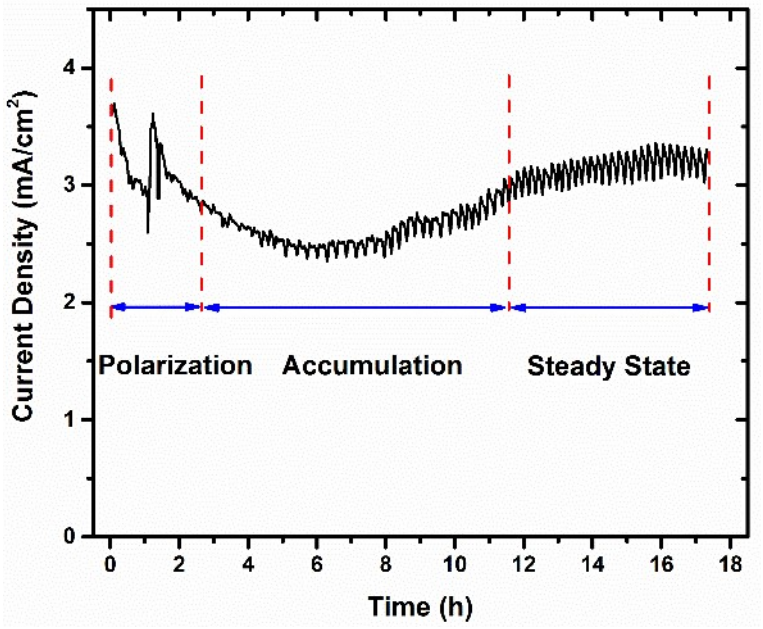

Fig. S21. Current density *vs*. Time for stability test of Zn-Cd heterojunction patch at 2.33 V *vs*. RHE, in a two-compartment cell, 2M $KHCO_3$, room temperature, and Pt as the counter electrode.

Fig. S22a-d represent the homogenous distribution of CdO nanodots on ZnO NWs. In contrast, **Fig. S22e-g** show the morphology of the ZnO-CdO sample after an extended stability test that clearly proves a significant reconstruction of the surface morphology. In addition, the EDS line scanning (**Fig. S22i**) and mapping (**Fig. S22j-n**) results of the Zn-Cd indicates the homogeneity of the CdO distribution on the Zn structure. It is noteworthy that the Sn-assigned peak in the EDS spectrum originates from the FTO substrate. These results confirm that the chemical composition remains almost similar to the as-synthesised patch while the morphology is remarkably reconstructed. We believe that transformation

from CdO to $CdCO_3$ in K_2CO_3 solution accelerates this reconstruction process at the beginning of the catalytic process. By the passage of time, ZnO NWs and $CdCO_3$ nanodots combine and contract to move toward geometry with the lowest surface energy (i.e., sphere). This attachment and growth theory is also presented in the studies conducted by Tuaev et al.[31] and Moriau et al.[32].

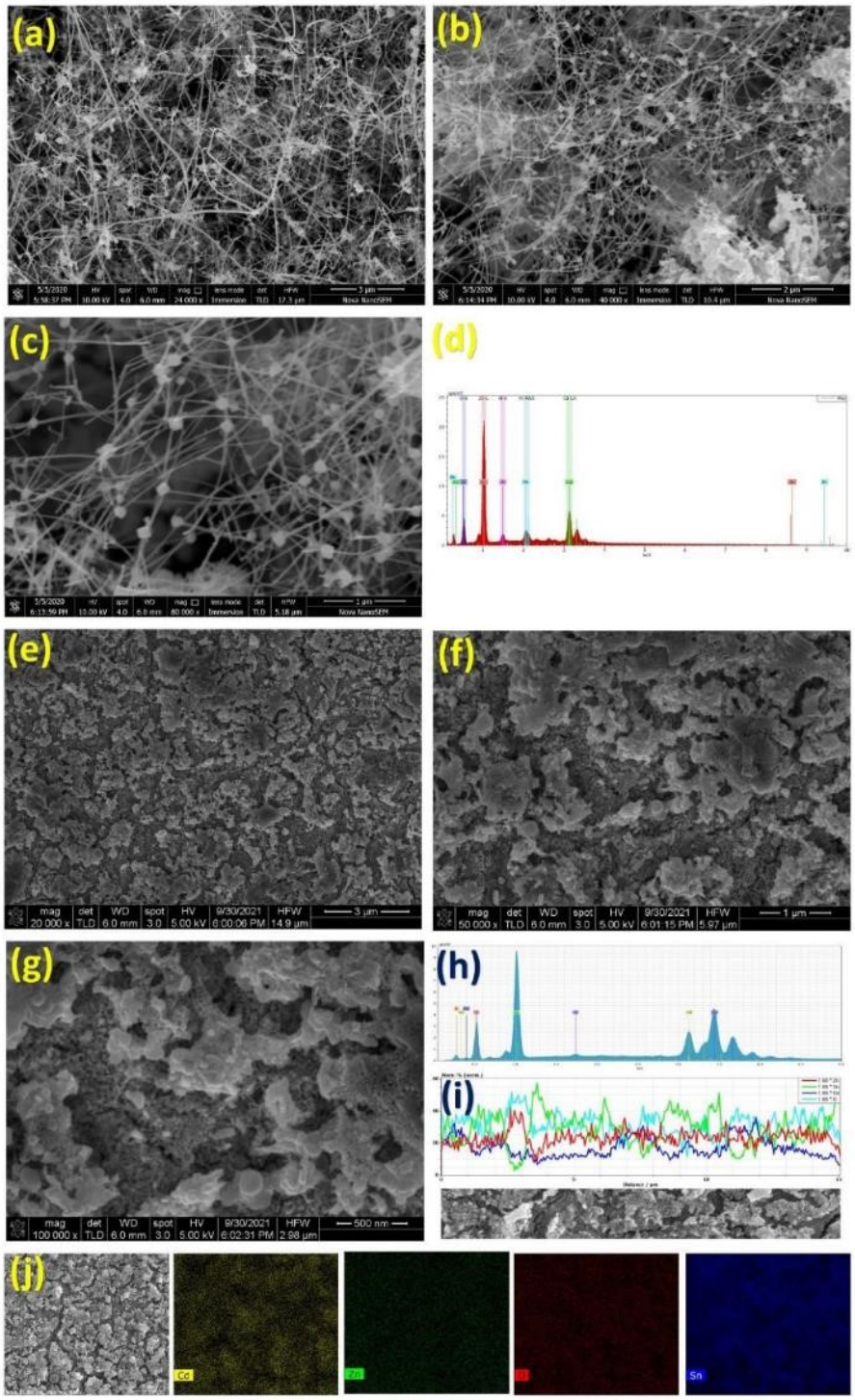

Fig. S22. (a)-(c) as-synthesised ZnO/CdO patch in different magnifications, **(d)** EDS map spectrum of image (a), indicating the copresence of Cd and Zn, **(e)-(g)** reconstructed surface of the ZnO/CdO sample after long term stability test in K_2CO_3 solution in different magnifications, **(h)** EDS map spectrum of image (e), **(i)** EDS line scanning of the sample with the reconstructed surface, and **(j)** EDS map analysis of the sample with the reconstructed surface, representing the distribution of Cd and Zn.

A major concern about Zn-Cd patch is the environmental hazard of Cd dissolution in the solution for long runs. **Fig. S23** shows the concentration of Cd, Zn, and Sn after around 20 h at 2.53 V vs. RHE. Clearly, the concentration of three elements are insignificant, commutatively less than 0.64 ppm before and after the test, signifying the lack of contamination of the solution by the catalysts (Zn-Cd).

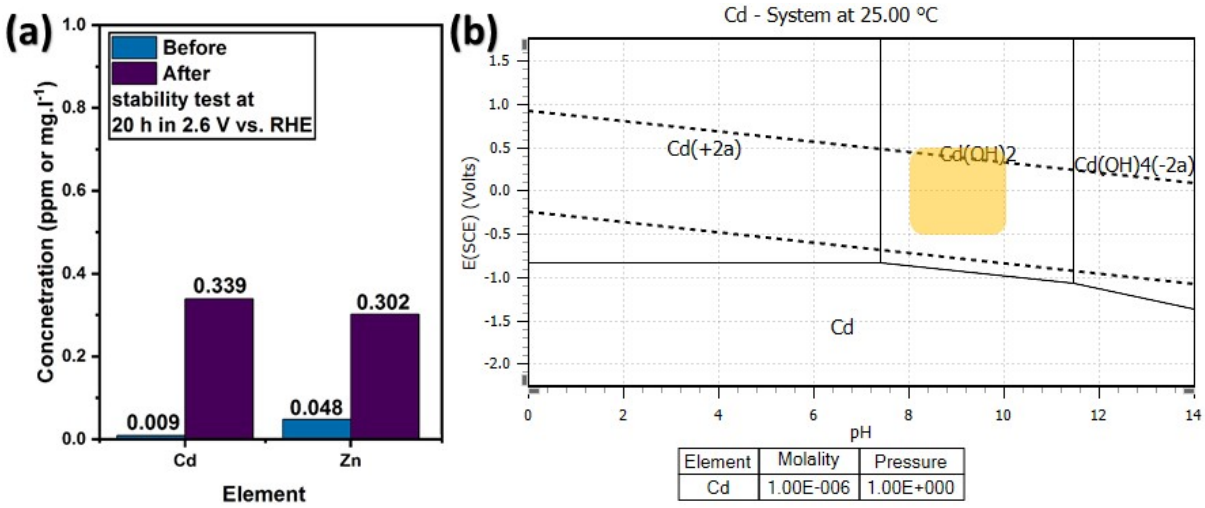

Fig. S23. (a) Change in the concentration of Cd, Zn, and Sn after the stability test of ZnO/CdO heterojunction patch at 2.53 V vs. RHE for 20 h, **(b)** Pourbaix diagram of Cd, where our working Eh-pH is shown in the yellow rectangle.

The highest FE at the accumulation test was around 20% after 3 h and passage of 32 C. Since H_2O_2 accumulation is a function of time, H_2O_2 decomposition and oxidative H_2O_2 formation compete with each other and affect the final H_2O_2 accumulation value. Rapid decomposition

of H_2O_2 after the formation at ambient temperature leads to misleading activity trends[18]; hence, the real generated H_2O_2 is more than detected. To alleviate this issue, the electrochemical cell is advised to cool down below 5°C[18]. HCO_3^- also can be detrimental in H_2O_2 accumulation owing to occurring Re. S3 in reverse according to Le Chatelier's principle[17]. It is reported that H_2O_2 accumulation on bare FTO and TiO_2 electrodes decreased with increasing applied electric charge and completely stopped at high applied electric charge[22].

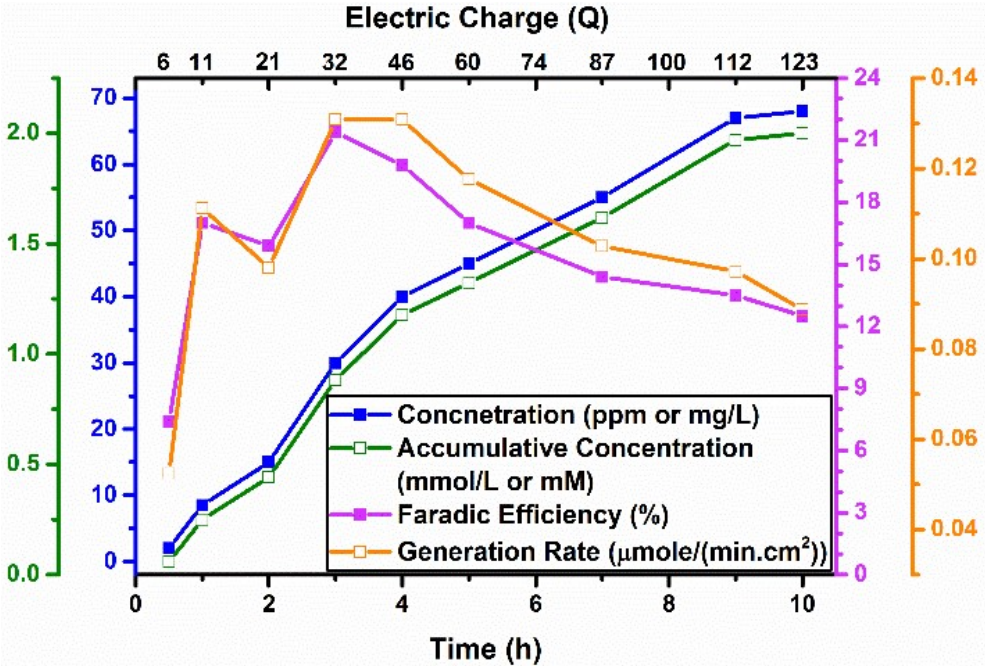

Fig. S24. Accumulated H_2O_2 and FE of Zn-Cd heterojunction patch *vs*. the passage of time at 2.33 V *vs*. RHE, in a two-compartment cell, 2M $KHCO_3$, room temperature, and Pt as the counter electrode.

Table S1. Summary of the thin film catalysts applied for electrochemical (EC) oxidative H_2O_2 generation in a two-compartment cell.

Cathode film	Cathode substrate	Anode material	Potential (V) vs. RHE	Electrolyte	H_2O_2 generation rate ($\mu mol.min^{-1}.cm^{-2}$)	Accumulated H_2O_2	Faradic Efficiency (%) of H_2O_2 generation	Onset* potential of WOR (V) vs. RHE	pH	Temperature (°C)	Ref.
$BiVO_4$	FTO	Ti foil	3.1	1 M $NaHCO_3$	5.8		70	2.1	8.3	Room Temperature	[21]
SnO_2	FTO	Ti foil	3.1	1 M $NaHCO_3$	1.5		51	2.22	8.3	Room Temperature	[21]
TiO_2	FTO	Ti foil	3.3	1 M $NaHCO_3$	1.0		18	2.35	8.3	Room Temperature	[21]
WO_3	FTO	Ti foil	2.3	1 M $NaHCO_3$	0.6		46	1.98	8.3	Room Temperature	[21]
$BiVO_4$	FTO	Pt mesh	3.0	0.5 M $KHCO_3$	71 µM/1.8C	5 mM at 7 V	35%	≈2.25	7.3	5	[22]
Bare FTO	-	Pt mesh	3.0	0.5 M $KHCO_3$	38 µM/1.8C		<35%	-	7.3	5	[22]
CoO	FTO	Pt mesh	3.0	0.5 M $KHCO_3$	1 µM/1.8C		<35%	-	7.3	5	[22]
WO_3	FTO	Pt mesh	3.0	0.5 M $KHCO_3$	32 µM/1.8C		<35%	-	7.3	5	[22]
La_2O_3	FTO	Pt mesh	3.0	0.5 M $KHCO_3$	23 µM/1.8C		<35%	-	7.3	5	[22]
Nb_2O_5	FTO	Pt mesh	3.0	0.5 M $KHCO_3$	26 µM/1.8C		<35%	-	7.3	5	[22]
Al_2O_3	FTO	Pt mesh	3.0	0.5 M $KHCO_3$	45 µM/1.8C		<35%	-	7.3	5	[22]
TiO_2	FTO	Pt mesh	3.0	0.5 M $KHCO_3$	73 µM/1.8C		<35%	-	7.3	5	[22]
ZrO_2	FTO	Pt mesh	3.0	0.5 M $KHCO_3$	32 µM/1.8C		<35%	-	7.3	5	[22]
V_2O_5	FTO	Pt mesh	3.0	0.5 M $KHCO_3$	36 µM/1.8C		<35%	-	7.3	5	[22]
Bi_2O_3	FTO	Pt mesh	3.0	0.5 M	12 µM/1.8C		<35%	-	7.3	5	[22]

				$KHCO_3$							
ZnO (nanorod)	FTO	Carbon paper	3.0	2 M $KHCO_3$	-		75	1.80	8.3	Room Temperature	[4]
ZnO (nanoparticle)	FTO	Carbon paper	3.0	2 M $KHCO_3$	-		60	≈2.0	8.3	Room Temperature	[4]
$CaSnO_3$	FTO	Carbon paper	3.2	2 M $KHCO_3$	4.6		76	1.99	8.3	Room Temperature	[3]
Bare FTO	-	Carbon paper	3.2	2 M $KHCO_3$	0.9		32	≈2.25	8.3	Room Temperature	[3]
SnO_2	FTO	Carbon paper	3.2	2 M $KHCO_3$	1.1		32	2.13	8.3	Room Temperature	[3]
Boron-doped Diamond	Ti plate	Pt mesh	3.17	2 M $KHCO_3$	19.7		28	≈2.65	8.0	Room temperature	[29]
PTFE-patterned glassy carbon (GC)	-	Pt foil		1 M Na_2CO_3	23.4		66	2.4	11.96	25	[33]
Bare glassy carbon	-	Pt foil		1 M Na_2CO_3	8.4		11		11.96	25	[33]
PTFE decorated carbon fibre paper (CFP)	-	Pt foil	2.4	1 M Na_2CO3	23.4			≈2.0	11.96	25	[28]
C, N codoped TiO_2			3.05	0.05 Na_2SO_4	0.29 $\mu mol.L^{-1}.cm^{-2}.h^{-1}$	1.7 $\mu mol.L^{-1}$ in 6 h at 3.29 V	8	3.05	3.0	25	
FTO	-	Pt wire	2.5-2.7 V under constant 0.33 mA/cm^2	0.5 M $KHCO_3$			13 at 1.8 C	2.25		5	[25]
$CuSb_2O_x$	FTO	Pt wire	2.5-2.7 V under constant 0.33 mA/cm^2	0.5 M $KHCO_3$			30 at 1.8 C	2.03		5	[25]
$InSbO_x$	FTO	Pt wire	2.5-2.7 V under	0.5 M $KHCO_3$			45 at 1.8 C	2.23		5	[25]

			constant 0.33 mA/cm^2								
$InSbO_x/CuSb_2O_x$	FTO	Pt wire	2.5-2.7 V under constant 0.33 mA/cm^2	0.5 M $KHCO_3$		5.7 mM at 3 V	53 at 1.8 C	2.04		5	[25]
$Al_2O_3/BiVO_4$	FTO	Pt wire	2.5-2.7 V under constant 0.33 mA/cm2	0.5 M $KHCO_3$		4 mM at 3 V	43 at 1.8 C			5	[25]
FTO	-	Pt wire	constant 0.33 mA/cm^2	0.5 M $KHCO_3$		3.1 mM at 4 V	13 at 3.5 C	≈2.45	7.1	5	[24]
Al_2O_3	FTO	Pt wire	constant 0.33 mA/cm^2	0.5 M $KHCO_3$			22 at 3.5 C	≈2.75	7.1	5	[24]
$BiVO_4$	FTO	Pt wire	constant 0.33 mA/cm^2	0.5 M $KHCO_3$		5 mM at 4 V	23 at 3.5 C	2.11	7.1	5	[24]
$Al_2O_3/BiVO_4$	FTO	Pt wire		0.5 M $KHCO_3$		7.5 mM at 4		2.11	7.1	5	[24]
CdO/ZnO heterojunction patch	FTO	Pt wire	2.33	2 M $KHCO_3$	2.5	2 mM at 2.33	20	1.91	8.3	Room Temperature	Present Work

*The potential at which catalyst achieves 0.2 $mA \cdot cm^{-2}$ regardless of the weight of the catalyst[21]

4. References

1 Z. W. Pan, Z. R. Dai and Z. L. Wang, Science, 2001, 291, 1947–1949.

2 Z. G. Ji, F. Hao, C. Wang and J. H. Xi, *Chinese Phys. Lett.*, 2008, **25**, 3467–3469.

3 S. Y. Park, H. Abroshan, X. Shi, H. S. Jung, S. Siahrostami and X. Zheng, *ACS Energy Lett.*, 2019, **4**, 352–357.

4 S. R. Kelly, X. Shi, S. Back, L. Vallez, S. Y. Park, S. Siahrostami, X. Zheng and J. K. Nørskov, *ACS Catal.*, 2019, **9**, 4593–4599.

5 C. Cazorla and J. Boronat, *Rev. Mod. Phys.*, 2017, **89**, 1–54.

6 J. P. Perdew, A. Ruzsinszky, G. I. Csonka, O. A. Vydrov, G. E. Scuseria, L. A. Constantin, X. Zhou and K. Burke, *Phys. Rev. Lett.*, 2008, **100**, 1–4.

7 R. A. Vargas-Hernández, *J. Phys. Chem. A*, 2020, **124**, 4053–4061.

8 P. E. Blöchl, *Phys. Rev. B*, 1994, **50**, 17953–17979.

9 E. N. Brothers, A. F. Izmaylov, J. O. Normand, V. Barone and G. E. Scuseria, J. Chem. Phys., 2008, 129, 011102.

10 Z. Liu, C. Menéndez, J. Shenoy, J. N. Hart, C. C. Sorrell and C. Cazorla, Nano Energy, 2020, 72, 104732.

11 Z. L. Wang, X. Y. Kong and J. M. Zuo, *Phys. Rev. Lett.*, 2003, **91**, 1–4.

12 St. Hovel, C. Kolczewski, M. Wu¨hn, J. Albers, K. Weiss, V. Staemmler, Ch. Woll, *J. Chem. Phys.*, 2000, **112**, 3909-3916 .

13 Y. Yu and B. Liu, *Phys. Rev. B*, 2008, **77**, 195327.

14 S. Siahrostami, A. Verdaguer-Casadevall, M. Karamad, D. Deiana, P. Malacrida, B. Wickman, M. Escudero-Escribano, E. A. Paoli, R. Frydendal, T. W. Hansen, I. Chorkendorff, I. E. L. Stephens and J. Rossmeisl, *Nat. Mater.*, 2013, **12**, 1137–1143.

15 X. Tan, H. A. Tahini and S. C. Smith, *Mater. Horizons*, 2019, **6**, 1409–1415.

16 V. Wang, N. Xu, J. C. Liu, G. Tang and W.-T. Geng, Comput. Phys. Commun., 2021, 267, 108033.17 J. Liu, Y. Zou, B. Jin, K. Zhang and J. H. Park, *ACS Energy Lett.*, 2019, **4**, 3018–3027.

18 K. Fuku and K. Sayama, *Chem. Commun.*, 2016, **52**, 5406–5409.

19 V. Viswanathan, H. A. Hansen and J. K. Nørskov, *J. Phys. Chem. Lett.*, 2015, **6**, 4224–4228.

20 S. C. Perry, D. Pangotra, L. Vieira, L. I. Csepei, V. Sieber, L. Wang, C. Ponce de León and F. C. Walsh, *Nat. Rev. Chem.*, 2019, **3**, 442–458.

21 X. Shi, S. Siahrostami, G. L. Li, Y. Zhang, P. Chakthranont, F. Studt, T. F. Jaramillo, X.

Zheng and J. K. Nørskov, *Nat. Commun.*, 2017, **8**, 1–12.

22 K. Fuku, Y. Miyase, Y. Miseki, T. Gunji and K. Sayama, *ChemistrySelect*, 2016, **1**, 5721–5726.

23 S. Siahrostami, S. J. Villegas, A. H. Bagherzadeh Mostaghimi, S. Back, A. B. Farimani, H. Wang, K. A. Persson and J. Montoya, *ACS Catal.*, 2020, 7495–7511.

24 Y. Miyase, S. Iguchi, Y. Miseki, T. Gunji and K. Sayama, *J. Electrochem. Soc.*, 2019, **166**, H644–H649.

25 Y. Miyase, Y. Miseki, T. Gunji and K. Sayama, *ChemElectroChem*, 2020, **7**, 2448–2455.

26 A. Izgorodin, E. Izgorodina and D. R. MacFarlane, *Energy Environ. Sci.*, 2012, **5**, 9496–9501.

27 S. G. Xue, L. Tang, Y. K. Tang, C. X. Li, M. L. Li, J. J. Zhou, W. Chen, F. Zhu and J. Jiang, *ACS Appl. Mater. Interfaces*, 2020, **12**, 4423–4431.

28 C. Xia, S. Back, S. Ringe, K. Jiang, F. Chen, X. Sun, S. Siahrostami, K. Chan and H. Wang, *Nat. Catal.*, 2020, **3**, 125–134.

29 S. Mavrikis, M. Göltz, S. Rosiwal, L. Wang and C. Ponce de León, *ACS Appl. Energy Mater.*, 2020, **3**, 3169–3173.

30 C. Wei, S. Sun, D. Mandler, X. Wang, S. Z. Qiao and Z. J. Xu, *Chem. Soc. Rev.*, 2019, **48**, 2518–2534.

31 X. Tuaev, S. Rudi and P. Strasser, *Catal. Sci. Technol*.,2016, **6**,8276–8288.

32 L. Moriau, M. Bele, Z. Marinko, F. Ruiz-zepeda, G. Podborsek, M. Sala, A. Surca, J. Kovac, I. Arcon, P. Jovanovic, N. Hodnik and and L. Suhadolnik, *ACS Catal.*, 2021, **11**, 670−681.

33 C. P. de León, *Nat. Catal.*, 2020, **3**, 96–97.